

Helicity and winding fluxes as indicators of twisted flux emergence

D. MACTAGGART^{†*} and C. PRIOR[‡]

[†]School of Mathematics and Statistics, University of Glasgow, Glasgow G12 8QQ, UK

[‡]Department of Mathematical Sciences, Durham University, Durham, DH1 3LE, UK

(Received 00 Month 20xx; final version received 00 Month 20xx)

Evidence for the emergence of twisted flux tubes into the solar atmosphere has, so far, come from indirect signatures. In this work, we investigate directly the topological input of twisted flux tube emergence by studying helicity and winding fluxes. In magnetohydrodynamic simulations with domains spanning from the top of the convection zone to the lower corona, we simulate the emergence of twisted flux tubes with a range of different initial field strengths. One important feature of this work is the inclusion of a convectively unstable layer beneath the photosphere. We find approximately self-similar behaviour in the helicity input for the different field strengths considered. As the tubes rise and reach the photosphere, there is a strong input of negative helicity since we consider left-handed twisted tubes. This phase is then followed by a reduction of the negative input and, for low initial field strengths, a net positive helicity input. This phase corresponds to the growing influence of convection on the field and the development of serpentine field structures during emergence. The winding flux can be used to detect when the twisted cores of the tubes reach the photosphere but this signature does not exhibit self-similar behaviour across the range of initial field strengths. In short, the helicity and winding fluxes can provide much information about how a magnetic field emerges that is not directly available from other sources, such as magnetograms.

Keywords: Magnetohydrodynamics, Magnetic helicity, Field line winding, Magnetic topology, Flux emergence

1. Introduction

The idea of magnetic flux tubes rising through the convection zone to form bipolar active regions is long-standing (e.g. Cowling 1946, Jensen 1955, Parker 1955). The magnetic field lines in a rising flux tube are, generally, considered to be highly twisted for the simple reason that a tube needs to survive the destructive effects of convection (e.g. Fan *et al.* 2003, Abbett *et al.* 2004, Bushby and Archontis 2012). Apart from this requirement, there is some observational evidence that suggests twisted flux tube emergence may be responsible for the formation of certain active regions (Poisson *et al.* 2015, 2016). In this paper we will assume that solar active regions are formed by twisted flux tubes that rise to the photosphere and describe procedures that can be used to test this assumption. For an alternative theory on active region formation see, for example, Brandenburg *et al.* (2010), Kemel *et al.* (2013) and Mitra *et al.* (2014).

Another appealing aspect of active regions being formed by twisted flux tubes is that twisted flux tubes provide an obvious source of magnetic helicity, which is important for the formation of eruptions. Since we cannot measure the magnetic field directly in the solar atmosphere, we require a robust method of indicating if strongly twisted magnetic field emerges. In this paper, we show that direct evidence of twisted flux tube emergence can be found by considering two quantities related to magnetic field topology: *helicity flux* and *winding flux*. The first of these quantities, the helicity flux, describes the amount of relative magnetic helicity passing through the photosphere and is used widely in both theoretical and observational studies (e.g. Berger 1984, 1988, Démoulin and Berger 2003, Prior and MacTaggart 2019, Pariat 2019). The second

*Corresponding author. Email: david.mactaggart@glasgow.ac.uk

quantity, the winding flux, is a purely topological quantity that represents the average winding of magnetic field lines. It is identical in form to the helicity flux except that the magnetic field weighting is removed. The winding can be used to quantify reconnective activity in magnetic fields (Prior and Yeates 2018). We will describe these quantities in more detail later.

Simulations of twisted flux tube emergence have typically led to single signs for both the helicity rate and the total helicity input through the photosphere (e.g. Yang *et al.* 2013, Moraitis *et al.* 2014, Sturrock and Hood 2016). However, helicity input time series calculated from photospheric vector magnetograms have typically shown a far more mixed behaviour. For example, there are cases of bipolar emergence whose net helicity input has a consistent sign but whose input rate can vary in sign, as in Kusano *et al.* (2002) and Chae *et al.* (2004), or even the case where the total helicity input varies in sign, such as in Chae (2001) and Vemareddy and Démoulin (2017). There is a clear need to attempt to explain this disparity through flux emergence simulations.

On this front, Prior and MacTaggart (2019) simulated the emergence of both twisted and ‘mixed helicity’ magnetic fields (fields with balanced but spatially varying negative and positive twisting). First, it was shown that in both cases mixed helicity input rates were possible. In the twisted tube case this was due to the core of the flux rope becoming trapped at the photosphere. In the mixed helicity case, it was due to a combination of the field’s inherently mixed topology as well as emergence and submergence events. A second important aspect of the results of Prior and MacTaggart (2019) was to demonstrate that an examination of the winding, both the time series and density maps, in conjunction with the helicity, allows for a much more detailed interpretation of behaviour at the photosphere. One particular result was a clear jump in the winding time series indicating the emergence of the twisted core of the flux tube above the photospheric boundary. This result is important as it provides a clear signal that magnetic field of substantial twist has entered the solar atmosphere, something that is not clear from only examining the helicity data or other sources, such as magnetograms.

In this paper, we extend the work of Prior and MacTaggart (2019) by including a convectively unstable solar interior. Since our focus is on the emergence of twisted flux tubes, we will be able to test if this field line topology, in conjunction with the effects of convection, is enough to lead to mixed sign helicity signatures. We also aim to describe what clear signatures (if any) arise in the helicity and winding data that can give a clear indication that significant twist has entered the solar atmosphere.

The outline of the paper is as follows, first, the main equations and simulation setup are described. This section is followed by a description of the helicity and winding fluxes. Then, the analyses of the simulations are presented in detail and the paper concludes with a summary and a discussion.

2. Simulation and initial condition setup

2.1. Main equations

To model the large-scale behaviour of an emerging active region, we solve the compressible and ideal MHD equations using a Lagrangian remap scheme Arber *et al.* (2001). In dimensionless form, the MHD equations are

$$\left(\frac{\partial}{\partial t} + \mathbf{u} \cdot \nabla \right) \rho = -\rho \nabla \cdot \mathbf{u}, \quad (1)$$

$$\rho \left(\frac{\partial}{\partial t} + \mathbf{u} \cdot \nabla \right) \mathbf{u} = -\nabla p + (\nabla \times \mathbf{B}) \times \mathbf{B} + \nabla \cdot \boldsymbol{\sigma} + \rho \mathbf{g}, \quad (2)$$

$$\left(\frac{\partial}{\partial t} + \mathbf{u} \cdot \nabla\right) \mathbf{B} = (\mathbf{B} \cdot \nabla) \mathbf{u} - (\nabla \cdot \mathbf{u}) \mathbf{B}, \quad (3)$$

$$\rho \left(\frac{\partial}{\partial t} + \mathbf{u} \cdot \nabla\right) \varepsilon = -p \nabla \cdot \mathbf{u} + Q_{\text{visc}} - \frac{\varepsilon - \varepsilon_0}{\tau}, \quad (4)$$

with specific energy density

$$\varepsilon = \frac{p}{(\gamma - 1)\rho}. \quad (5)$$

The basic variables are the density ρ , the pressure p , the magnetic induction \mathbf{B} (referred to as the magnetic field) and the velocity \mathbf{u} . The gravitational acceleration is denoted \mathbf{g} (uniform in the z -direction) and $\gamma = 5/3$ is the ratio of specific heats. The dimensionless temperature T can be found from

$$T = (\gamma - 1)\varepsilon. \quad (6)$$

The variables are made dimensionless against photospheric values, namely, pressure $p_{\text{ph}} = 1.4 \times 10^4$ Pa; density $\rho_{\text{ph}} = 2 \times 10^{-4}$ kg m $^{-3}$; scale height $H_{\text{ph}} = 170$ km; surface gravity $g_{\text{ph}} = 2.7 \times 10^2$ m s $^{-2}$; speed $u_{\text{ph}} = 6.8$ km s $^{-1}$; time $t_{\text{ph}} = 25$ s; magnetic field strength $B_{\text{ph}} = 1.3 \times 10^3$ G and temperature $T_{\text{ph}} = 5.6 \times 10^3$ K. In the non-dimensionalization of the temperature we use a gas constant $\mathcal{R} = 8.3 \times 10^3$ m 2 s $^{-2}$ K $^{-1}$ and a mean molecular weight $\tilde{\mu} = 1$. The fluid viscosity tensor and the viscous contribution to the energy equation are respectively

$$\boldsymbol{\sigma} = 2\mu \left[\mathbf{D} - \frac{1}{3}(\text{tr} \mathbf{D}) \mathbf{I} \right] \quad \text{and} \quad Q_{\text{visc}} = \boldsymbol{\sigma} : \nabla \mathbf{u}, \quad (7)$$

where

$$\mathbf{D} = \frac{1}{2} (\nabla \mathbf{u} + \nabla \mathbf{u}^T) \quad (8)$$

is the symmetric part of the rate of strain tensor and \mathbf{I} is the identity tensor. We take $\mu = 10^{-4}$ and use this form of viscosity primarily to aid stability. The code accurately resolves shocks by using a combination of shock viscosity (Wilkins 1980) and Van Leer flux limiters (Van Leer 1979), which add heating terms to the energy equation. From now on, values will be expressed in non-dimensional form unless explicitly stated otherwise.

The last term in equation (4) represents the non-adiabatic contribution to the energy of the plasma. Following Leake and Arber (2006), we model this complex collection of physical phenomena using a simple Newton cooling term throughout the domain above the photosphere (see below for how the photospheric boundary is defined). The purpose of this term is to preserve the photosphere from being destroyed by the solar interior, which is convectively unstable (we will return to this point shortly). At $t = 0$ of the simulation, $\varepsilon = \varepsilon_0$ and the Newton cooling term forces the energy profile above the photosphere to return to this initial state on a fast time scale of $\tau = 0.5$.

2.2. Initial conditions

2.2.1. Background atmosphere and convective perturbation

At the start of the simulations, the computational domain is filled by a plane-parallel atmosphere that represents the solar atmosphere ranging from the top of the solar interior (convection zone) to the corona. The temperature profile above the lower boundary of the photosphere ($z = 0$) is given by

$$T(z) = \begin{cases} 1, & 0 \leq z \leq 10, \\ 150^{[(z-10)/10]}, & 10 < z < 20, \\ 150, & z \geq 20, \end{cases} \quad (9)$$

where the three rows in equation (9) correspond to the photosphere/chromosphere, the transition region and the corona respectively. The other state variables, pressure and density, are found by solving the hydrostatic equation in conjunction with the ideal equation of state

$$\frac{dp}{dz} = -\rho g, \quad p = \rho T. \quad (10)$$

The initial atmosphere described above is common to many idealized flux emergence simulations (Hood *et al.* 2012). In this study, we also consider a solar interior that is convectively unstable. To achieve this in our idealized setup, the Schwarzschild condition (e.g. Archontis and Hood 2009, Priest 2014) states that a convective instability will set in for an adiabatic fluid if the following criterion (written in our notation) is satisfied,

$$-\frac{dT}{dz} > \frac{\gamma - 1}{\gamma}. \quad (11)$$

In the solar interior ($z < 0$) we consider an initial temperature profile of

$$T_{\text{si}}(z) = 1 - \delta z \frac{\gamma - 1}{\gamma}, \quad (12)$$

where δ is a non-dimensional parameter used to satisfy condition (11). In this paper we take $\delta = 1.3$ as this value leads to convection that has velocity magnitudes that are close to those of solar convection.

Our purpose here is to investigate, incrementally, the effect of convection on topological signatures and compare the results to previous work in Prior and MacTaggart (2019) where convection is not included. We excite a stable mode of convection with hexagonal cells based on the solution in Christopherson (1940) (see also Chandrasekhar (1961)). At $t = 0$, the velocity is perturbed as

$$u_z = \frac{3}{10} \exp(-(z + 5)^2) \left(\frac{1}{54\sqrt{3}} \cos(2\pi x) \cos(2\pi y) + \frac{1}{18} \cos(4\pi y) \right). \quad (13)$$

This perturbation acts below the photospheric boundary at $z = -5$ and the hexagonal cells of Christopherson's solution develop quickly in the solar interior. The numerical parameters in equation (13) are chosen to produce convection cells with typical solar values, i.e. speeds of $O(1)$ km s⁻¹ and sizes of $O(1)$ Mm.

2.2.2. Magnetic field

To model a magnetic flux tube, we adopt the standard profile for a cylindrical flux tube with uniform twist (e.g. Fan 2001). In cylindrical coordinates (r, θ, y) , with $r^2 = x^2 + (z - z_{\text{axis}})^2$, the magnetic field components are

$$B_r = 0, \quad B_y = B_0 \exp(-r^2/d^2), \quad B_\theta = \alpha r B_y, \quad (14)$$

where B_0 is the axial field strength, d is the flux tube radius and α is the field line twist. In this paper, we fix $d = 3$ and $\alpha = -0.4$ (left-handed twist). We consider a range of field strengths $B_0 = 3, 5$ and 7 .

The magnetic field in (14) is not force-free and is balanced by a pressure gradient, i.e.

$$\nabla p_m = (\nabla \times \mathbf{B}) \times \mathbf{B}, \quad (15)$$

where p_m is an additional pressure compared to the background hydrostatic pressure p_b such that $p = p_b + p_m$. For the magnetic field in (14), the additional pressure has the form

$$p_m = \frac{1}{4} B_0^2 \exp(-2r^2/d^2)(\alpha^2 d^2 - 2 - 2\alpha^2 r^2). \quad (16)$$

In order to make the flux tube rise up buoyantly towards the photosphere, we introduce a density deficit within the tube of the form

$$\frac{\rho_m}{\rho_b} = \frac{p_m}{p_b} \exp(-y^2/\lambda^2), \quad (17)$$

where the ρ_m is the density deficit, ρ_b is the background hydrostatic density and λ is a parameter that allows the flux tube to rise in the shape of an Ω -loop. Here we fix $\lambda = 20$.

The flux tube is placed initially at $z_{\text{axis}} = -15$. Since the density deficit is proportional to B_0^2 , the rise times will vary for the values that we consider. The initial position of the tube axis is deep enough, however, for the flux tube to encounter fully developed convection before reaching the photosphere.

2.2.3. Simulation parameters

All the simulations we present have a computational domain of size $(x, y, z) \in [-80, 80] \times [-80, 80] \times [-30, 80]$ with a resolution of 432^3 . These values are suitable for studying the initial emergence of the flux tubes and their growth into the corona. The simulations are stopped before the expanding magnetic field reaches the side boundaries. The boundary conditions are periodic on the side boundaries and closed on the top and bottom boundaries. A damping layer is placed near the top boundary to help prevent the reflection of waves generated by convection at the photosphere.

3. Helicity and winding fluxes

3.1. Basic definitions

The formula for the flux of relative helicity H through a planar boundary P is

$$\frac{dH}{dt} = -\frac{1}{2\pi} \int_{P \times P} B_z(\mathbf{a}_1) B_z(\mathbf{a}_2) \frac{d\theta}{dt} d^2 a_1 d^2 a_2, \quad (18)$$

where the angle θ between points $\mathbf{a}_1, \mathbf{a}_2 \in P$ is

$$\theta = \arctan \left[\frac{(\mathbf{a}_2 - \mathbf{a}_1) \cdot \mathbf{e}_y}{(\mathbf{a}_2 - \mathbf{a}_1) \cdot \mathbf{e}_x} \right] \quad (19)$$

and $\{\mathbf{e}_x, \mathbf{e}_y, \mathbf{e}_z\}$ is a basis of Cartesian space with \mathbf{e}_z normal to P . The position \mathbf{a} of a magnetic field line intersecting P and satisfying ideal MHD is given by

$$\frac{d\mathbf{a}}{dt} = \mathbf{u}_{\parallel} - \frac{u_z}{B_z} \mathbf{B}_{\parallel} = \mathbf{u}_{\parallel} - u_z \left(\frac{d\mathbf{a}}{dz} \right)_{\parallel}, \quad (20)$$

where \mathbf{u}_{\parallel} and \mathbf{B}_{\parallel} are the projections of \mathbf{u} and \mathbf{B} onto P .

Equation (18) is discussed at length, including its derivation and interpretation, in many other works (Berger 1984, Pariat *et al.* 2005, Prior and MacTaggart 2019). In short, however, equation (18) represents the rate of field line entanglement weighted by magnetic flux.

Analogous to equation (18) is the definition of the winding flux,

$$\frac{dL}{dt} = -\frac{1}{2\pi} \int_{P \times P} \sigma_z(\mathbf{a}_1) \sigma_z(\mathbf{a}_2) \frac{d\theta}{dt} d^2 a_1 d^2 a_2, \quad (21)$$

where

$$\sigma_z(\mathbf{x}) = \begin{cases} 1 & \text{if } B_z(\mathbf{x}) > 0, \\ -1 & \text{if } B_z(\mathbf{x}) < 0, \\ 0 & \text{if } B_z(\mathbf{x}) = 0. \end{cases} \quad (22)$$

Similar to the helicity flux, the rate dL/dt measures the change of field line entanglement passing through P . However, unlike dH/dt , the winding rate is not weighted by magnetic flux and thus represents a purely topological measure of the magnetic field. For example, consider a magnetic field with a complex field line topology but with very weak field strength. The helicity of such a magnetic field could be low but its winding high since the winding does not ‘read’ the field strength.

Although the winding can pick up more topological detail than the helicity, there is the danger it that picks up weak field with complex topology that does not play a significant dynamical role (such field would be essentially ignored by helicity due to the weak field strength). In practice, it is important to test winding results against cut-off values in order to determine if results are dynamically important. Therefore, equation (22) is modified to

$$\sigma_z(\mathbf{x}) = \begin{cases} 1 & \text{if } B_z(\mathbf{x}) > 0 \text{ and } |\mathbf{B}| > \epsilon, \\ -1 & \text{if } B_z(\mathbf{x}) < 0 \text{ and } |\mathbf{B}| > \epsilon, \\ 0 & \text{if } B_z(\mathbf{x}) = 0 \text{ or } |\mathbf{B}| \leq \epsilon. \end{cases} \quad (23)$$

where ϵ is a chosen cut-off. In this paper, we will consider a cut-off of $\epsilon = 0.01$. Even with cut-off values, the analysis of the winding flux must be performed with care, as will be made apparent when we describe the simulation analysis.

3.2. Related quantities

The helicity and winding rates of equations (18) and (21) respectively provide time series data. Times series of the actual helicity and winding input can be produced from the time integration of the rates, i.e.

$$H(t) = \int_{t_0}^t \frac{dH}{dt'} dt', \quad L(t) = \int_{t_0}^t \frac{dL}{dt'} dt' \quad (24)$$

Spatial information about the distribution of helicity and winding can be found by determining the contribution of one point $\mathbf{a}_0 \in P$ to the rate. Since \mathbf{a}_0 represents the intersection of a field line with P , this quantity represents the contribution of one field line to the helicity or winding input rate. Repeating this calculation for a large set of \mathbf{a}_0 produces a map of how the helicity or winding rate is distributed spatially. For helicity, the field line helicity input rate is

$$\frac{d\mathcal{H}}{dt}(\mathbf{a}_0) = -\frac{1}{2\pi} B_z(\mathbf{a}_0) \int_P B_z(\mathbf{a}) \frac{d\theta}{dt}(\mathbf{a}_0, \mathbf{a}) d^2a, \quad (25)$$

and, similarly, for the winding rate,

$$\frac{d\mathcal{L}}{dt}(\mathbf{a}_0) = -\frac{1}{2\pi} \sigma_z(\mathbf{a}_0) \int_P \sigma_z(\mathbf{a}) \frac{d\theta}{dt}(\mathbf{a}_0, \mathbf{a}) d^2a. \quad (26)$$

There are a number of additional analyses that we could potentially perform on the distributions (25) and (26) such as combining components through field line connectivity. However, they do not feature in our analysis here for reasons discussed in detail in Prior and MacTaggart (2019).

3.3. Accounting for a changing photosphere

Following Prior and MacTaggart (2019), we calculate approximate helicity and winding fluxes by projecting values from a non-planar and evolving photosphere onto P . This process is intended to mimic what actual observations are recording. In Prior and MacTaggart (2019), the photospheric boundary was taken to be the surface where $\rho = 1$, which represents the photosphere in the initial condition. As the simulation evolved and the flux tube emergence led to the rise and churn of dense plasma from below the location of the initial $\rho = 1$ surface, the surface became deformed. The field was sampled on this evolving surface and then projected onto P to represent the production of planar vector magnetograms used in observational helicity studies.

Due to the inclusion of convection in this study, this simple approach is no longer applicable as the $\rho = 1$ surface can become multi-valued. To account for this multi-valued structure and the fact the photosphere is really a thin volume instead of a surface (with a depth of approximately 100 km (Muller 1975)), we calculate ‘photospherically averaged’ magnetic field values as

$$\widehat{\mathbf{B}}(x, y) = \frac{\int_{z_{\min}}^{z_{\max}} \exp[-2(\rho - 1)^6] \mathbf{B}(x, y, z) dz}{\int_{z_{\min}}^{z_{\max}} \exp[-2(\rho - 1)^6] dz}, \quad (27)$$

and similarly for the velocity field. The idea is that the above average is calculated for a range of values whose density is suitably close to $\rho = 1$. The exponential weighting is chosen so that the density values that affect the average significantly are those that, with respect to the initial condition (determined by equation (9) in conjunction with equations (10)), correspond (approximately) to a vertical extent of 100km which contains $\rho = 1$ at its centre. The domain $[z_{\min}, z_{\max}]$ is chosen here to be $[-7.5, 7.5]$, i.e. suitably large to always contain the required density range. Whilst the photospheric domain deforms (and its vertical width varies) it corresponds to a consistent range of densities. In what follows we drop the hat from equation (27). It will be assumed, unless stated otherwise, that the magnetic and velocity fields used to construct the time series inputs (18), (21), (24) and the distributions (25), (26) are averages, calculated using (27). For comparison, in the $B_0 = 3$ simulation, we calculate a non-varying equivalent $\mathbf{B}^F = \mathbf{B}(x, y, 0)$ which ignores the varying density of the plasma. When this field choice is used it will be made explicitly clear.

4. Simulation analysis

We now present a detailed analysis of the simulations, considering each initial field strength in turn. Since there are similarities between the cases, we will describe the $B_0 = 7$ case in detail and only focus on specific highlights and differences for the $B_0 = 3, 5$ cases. For the basic properties of flux emergence, we refer the reader to the reviews by Hood *et al.* (2012) and Cheung and Isobe (2014). Our focus here is on how to interpret the topological signatures associated with emergence.

4.1. $B_0 = 7$, $\alpha = -0.4$

The helicity input rate dH/dt is shown in Figure 1(a). For most of the emergence period shown, the input is negative. This result is to be expected for a left-handed twisted flux rope. After $t = 65$, however, the rate is overall positive. This input pattern has the obvious effect of inputting overall negative helicity into the atmosphere as indicated in Figure 1(b).

The winding input rate dL/dt , shown in Figure 1(c), is on average negative with a number of sharp spikes whose origin we will characterize shortly. The result is a net input of negative

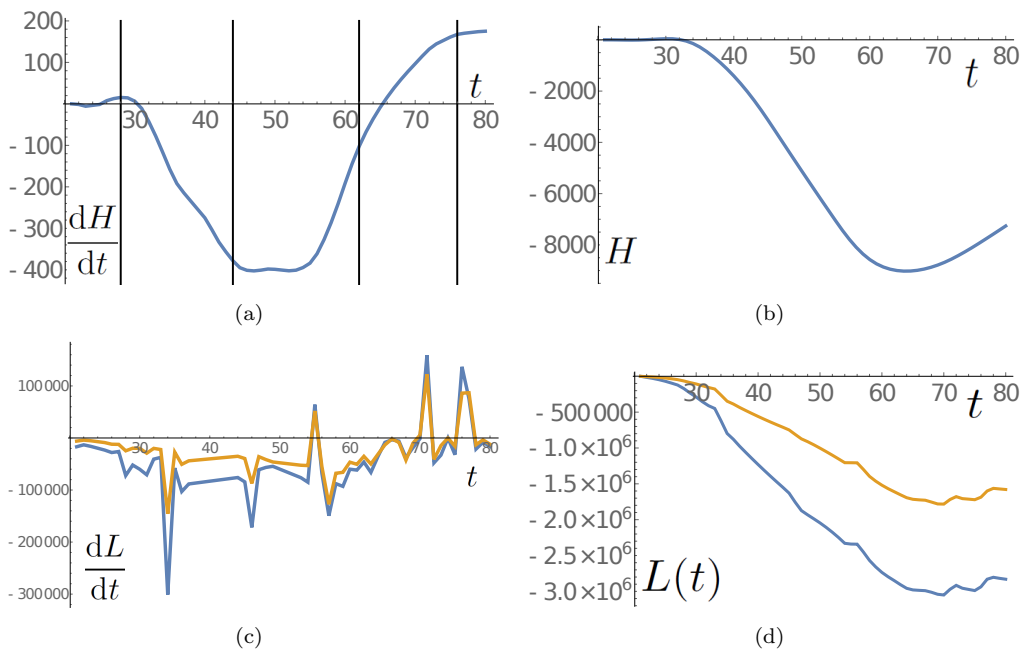


Figure 1. Helicity and winding time series for the $B_0 = 7 \alpha = -0.4$ case. Panel (a) shows the helicity input rate dH/dt . The vertical lines indicate times at which maps of $d\mathcal{H}(\mathbf{a}_0)/dt$ are plotted in Figure 4. Panel (b) shows the integrated helicity $H(t)$ over the same period. Panel (c) displays the winding input rate dL/dt with no cut-off (blue) and with a cut-off below $|B_z| = 0.01$ (brown). Panel (d) displays the total winding input $L(t)$.

winding consistent with the field’s structure (see the time series of $L(t)$ in Figure 1(d)). Both winding time series, with and without the cut-off $|B_z| = 0.01$, are shown. These two series are qualitatively similar with the magnitudes of values in the series with the cut-off being smaller.

Before investigating what causes the particular features in the time series in Figure 1, we will compare these results to those of Prior and MacTaggart (2019) where twisted flux tube emergence was studied in an atmosphere with a convectively stable solar interior. Making this comparison will help us assess the effects of convection on the topological signatures.

First, we point out that the magnetic field model used in this paper is different to that used in Prior and MacTaggart (2019). Here, a cylindrical tube is used rather than a toroidal tube. Although the emergence behaviours of these two magnetic field models are different (MacTaggart and Hood 2009), we will show that convection plays a fundamental role in determining the shape of the time series. For the benefit of the reader, let us recap briefly the main results for twisted tube emergence from Prior and MacTaggart (2019) (see their Figure 11 in particular). First, the helicity rate exhibited an oscillatory character that was due to the flux rope core oscillating at the photosphere. The helicity input continued to become more negative in time. The winding rate contained small oscillations and one significant spike. The winding input had a ‘step function’ profile meaning that once most the twisted core of the flux tube emerged, there was little new topological complexity input into the atmosphere after this event. With the above picture in mind, we will now investigate how the time series in Figure 1 differ from this picture.

Snapshots of the field at various times during its emergence are shown in Figure 2. At $t = 30$ (Figures 2(a) and (b)) the field is seen to have only just emerged above the $\rho = 1$ surface. By $t = 50$, the field has emerged much further into the atmosphere. Figure 2(c) shows a sheared arcade and Figure 2(d) indicates that convection has begun to affect the flux tube field lines significantly. At $t = 80$, in Figures 2(e) and (f), we see that the field has developed a strong ‘serpentine’ structure with field lines submerging and re-emerging at several points.

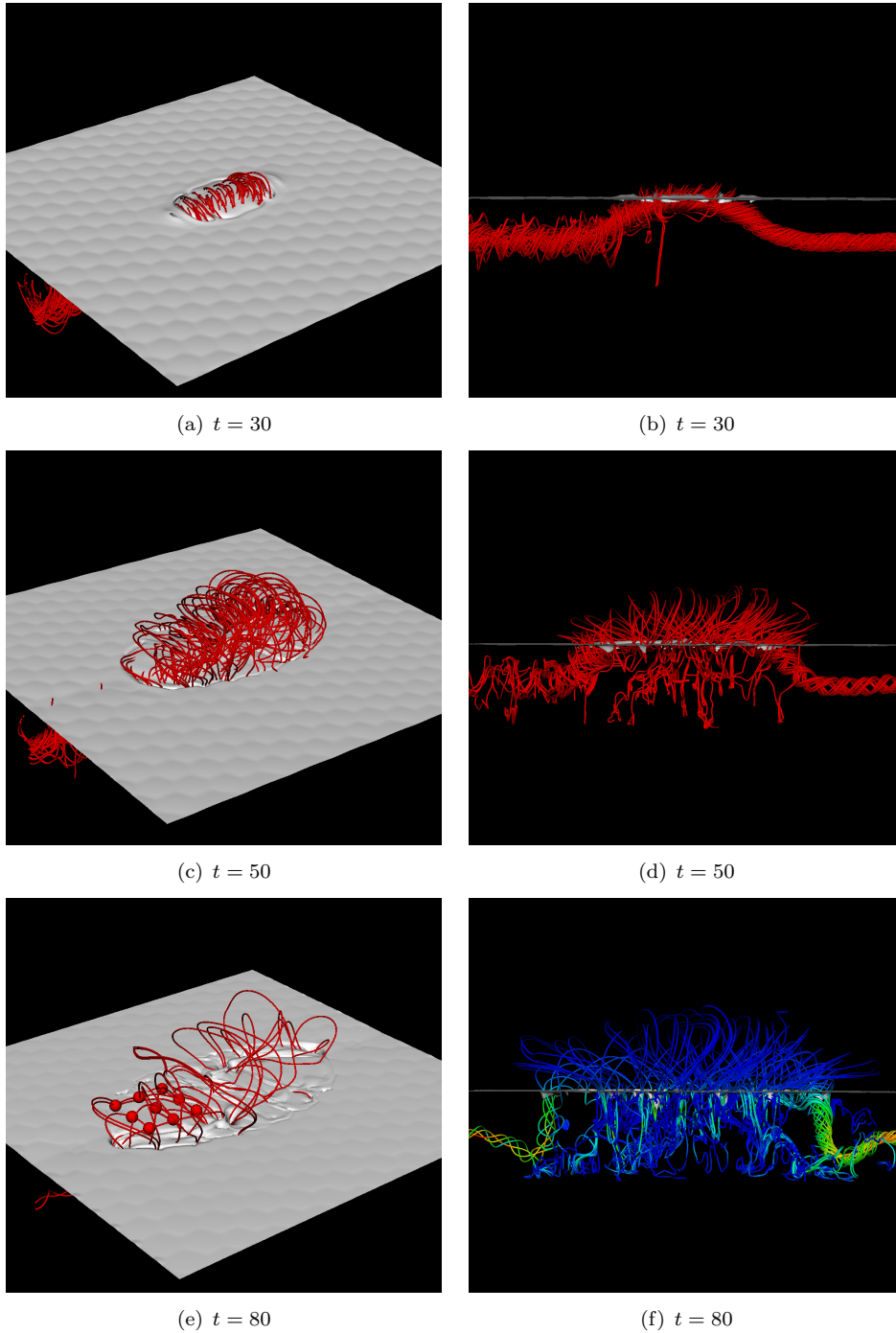


Figure 2. Field line renderings for the $B_0 = 7 \alpha = -0.4$ case at various points in its evolution. Panels (a) and (b) depict the field at $t = 30$. In (a) the surface shown is that of the plasma density $\rho = 1$. Panels (c) and (d) depict the field at $t = 50$. Panel (e) depicts field lines in the emerged field at $t = 80$. The spheres shown are the starting points for the field line integration. Panel (f) depicts field lines side-on, with lighter colours indicating increased field strength.

This behaviour is commonly observed in nonlinear force-free coronal field extrapolations (e.g. Pariat *et al.* 2004, Pariat *et al.* 2009, Harra *et al.* 2010, Valori *et al.* 2012) and is highlighted in Figure 2(e) which shows seed points at one side of the region and field lines, emanating from these point, submerging and emerging throughout the active region. The serpentine behaviour is further indicated in Figure 2(f) where the field lines are coloured by field strength and several loops of significantly strong field strength are present below the photosphere. Such behaviour

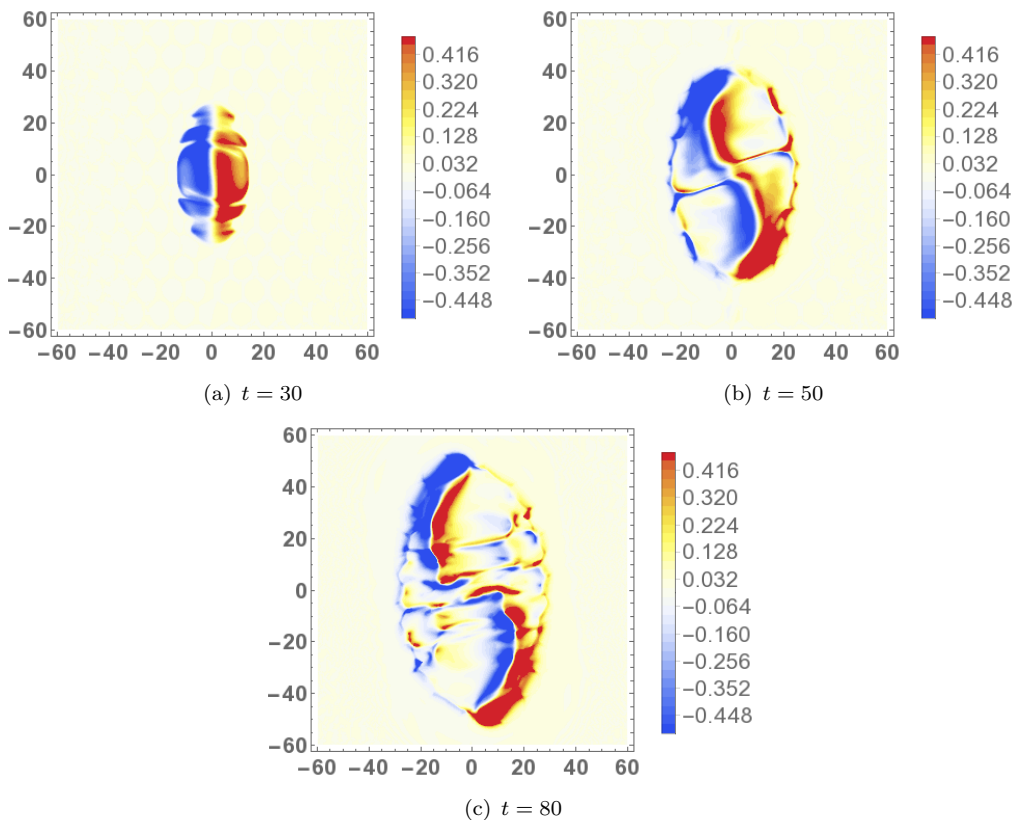


Figure 3. Magnetograms of the field at the surface $\rho = 1$ at the times shown in Figure 2.

is not found in non-convective simulations.

Magnetograms (of B_z) of the emerging field, at the times shown in Figure 2, are displayed in Figure 3. These magnetograms exhibit many features that are similar to those from non-convective simulations. There are, however, some important differences due to convection. At $t = 30$ in Figure 3(a), the field has just reached above the photosphere and there is no clear signal of twisted field. There is some disruption of the field due to convection cells. By $t = 50$ in Figure 3(b), the sigmoidal pattern (e.g. Fan and Gibson 2004, Archontis *et al.* 2009) of the twisted field has emerged and some disruption due to convection is evident (particularly around the edge of the region). At $t = 80$ in Figure 3(c), we see many more smaller-scale positive and negative flux features surrounding the sigmoid, indicative of the serpentine behaviour displayed in Figure 2.

To summarize the results so far, as the field emerges through the photosphere and expands into the atmosphere, it becomes more susceptible to deformation by convection (since the field strength is, overall, becoming weaker). The action of convection is to create a serpentine structure by pulling loops of magnetic field beneath the photosphere. Evidence for this behaviour is shown in field line plots (Figure 2) and magnetograms (Figure 3). The question now is how to relate this behaviour to the topological information given in Figure 1? To proceed, we will focus on the helicity first and then the winding.

4.1.1. Helicity evolution

The helicity time series in Figures 1(a) and (b) differ substantially from those for non-convective simulations (e.g. Sturrock and Hood 2016, Prior and MacTaggart 2019). Whereas for the non-convective case helicity continues to become more negative despite an oscillation about this mean trend, the helicity input in the convective case eventually stops becoming more negative and changes direction, becoming more positive. The time scale of this turning

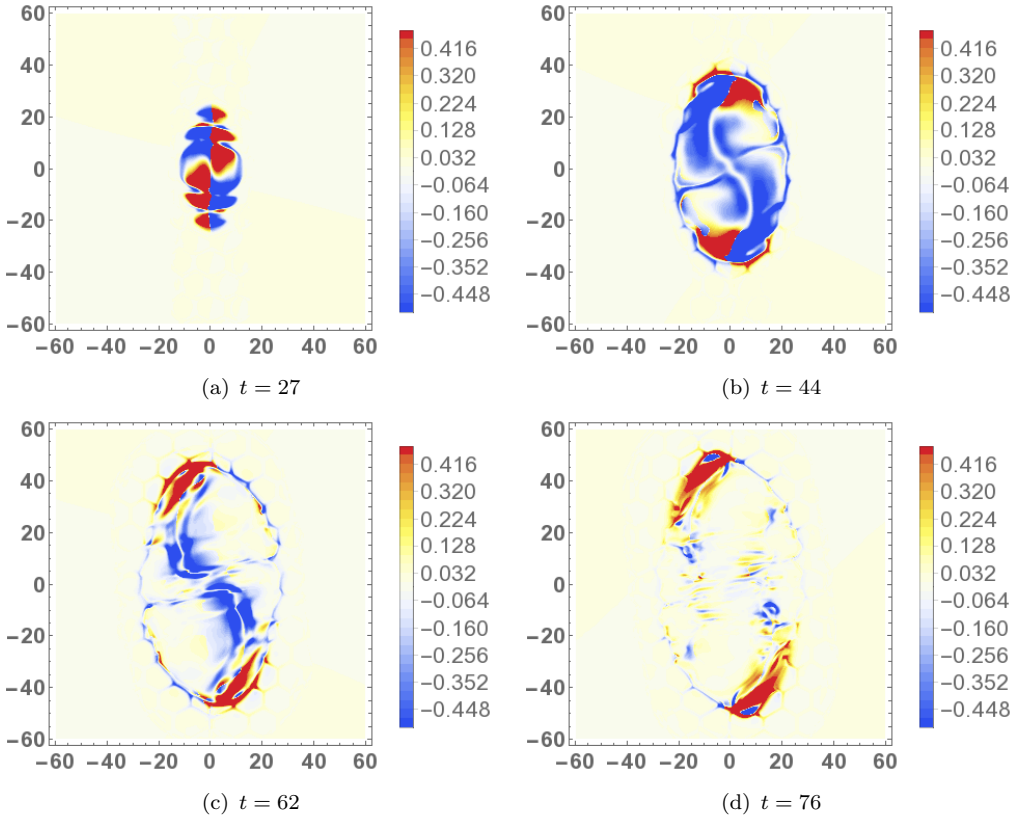


Figure 4. Helicity input rate distributions $d\mathcal{H}(\mathbf{a}_0)/dt$ at the times indicated by vertical lines in the helicity rate time series shown in Figure 1(a), i.e. $t = 27$ (a), $t = 44$ (b), $t = 62$ (c) and $t = 76$ (d).

point in the helicity flux coincides with the development of serpentine field lines driven by convection. By examining specific features in detail, we will now show that convection is ultimately responsible for the turning point in the helicity time series.

Figure 4 shows the field line helicity rate distributions $d\mathcal{H}(\mathbf{a}_0)/dt$ for times representing key phases in the helicity evolution. Figures 4(a-c) reveal an evolution that is similar qualitatively to that found in non-convective simulations. As the magnetic field first reaches the photosphere (Figure 4(a)), there is an approximate balance of positive and negative helicity (although in this case, convection helps to create a slight bias of positive helicity). Later (Figure 4(b)), as emergence of the tube with left-handed twist proceeds, the helicity rate distribution is dominated, naturally, by negative helicity. Later still (Figure 4(c)), the twisted core of the flux tube reaches the photosphere and this feature dominates the negative helicity rate signature. Although the band of negative helicity rate density, representing the twisted core, follows the sigmoidal polarity inversion line clearly, it also shows locations of disruption, particularly near $(0,0)$. At $t = 76$ (Figure 4(d)) the band of negative helicity rate density has been distorted significantly, although the regions of positive helicity rate density at $y = \pm 40$ persist. To investigate what causes the features in the helicity rate map in Figure 4(d), we investigate the behaviour of other quantities in the locations of particular helicity features.

Figure 5 displays slices (the x - z plane) of various quantities at $y = 30$ and $t = 76$, corresponding to a region of strong positive helicity rate (as shown in Figure 4(d)). Figure 5(a) displays a map of $\mathbf{e}_y \cdot \nabla \times \mathbf{B}$, vector arrows of the in-plane magnetic field and photospheric boundaries corresponding to $\rho = 1$ (green) and $\rho = 0.8, 1.2$ (cyan). The twisted core of the emerged flux tube can be seen far above the photospheric boundary in Figure 5(a). Just below the photospheric boundary at $x \approx -15$, there are strong currents of both signs. Further left

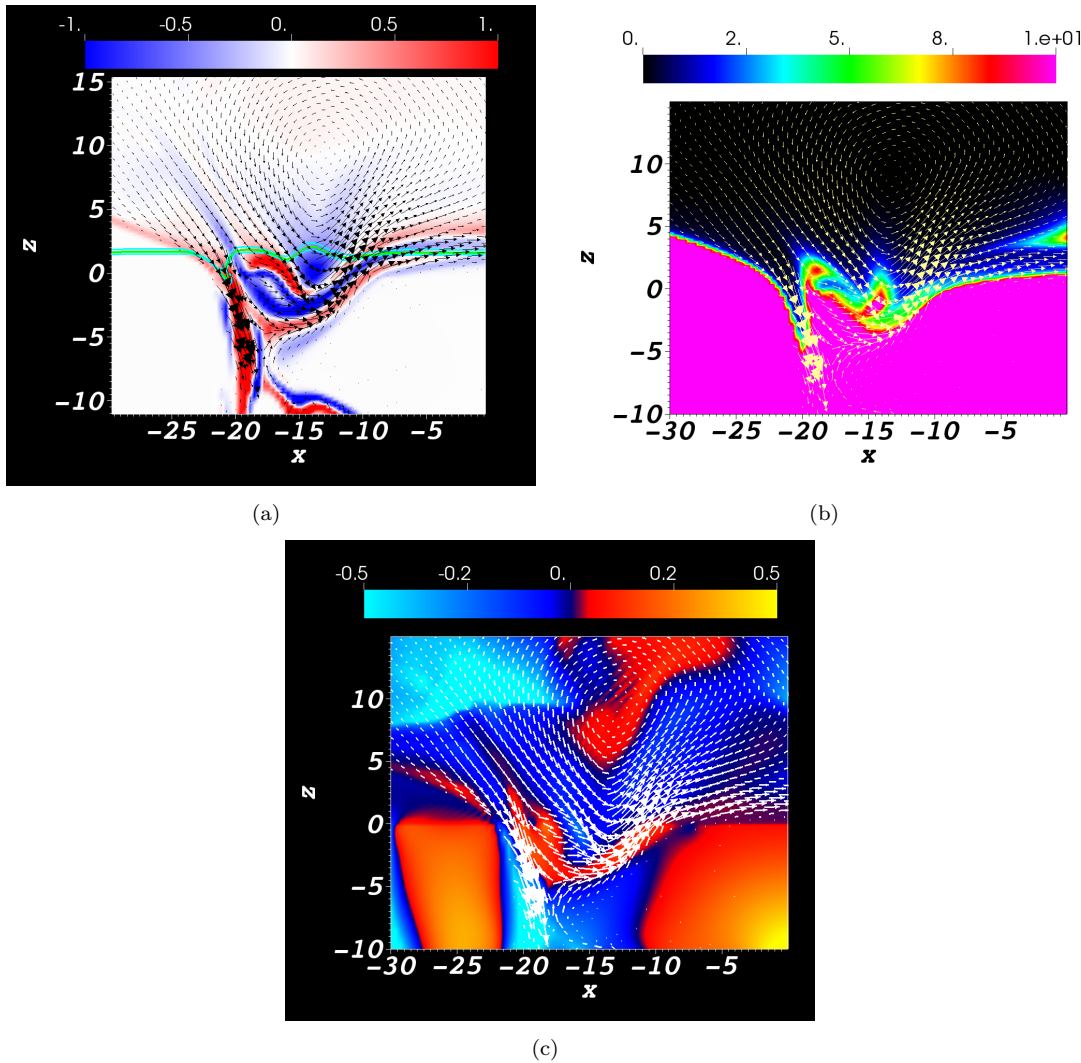


Figure 5. Slices at $t = 76$ taken in the x - z plane at $y = 30$ which intersects a region of strong positive helicity input rate $d\mathcal{H}(\mathbf{a}_0)/dt$ in Figure 4(d). In (a), a map of the y -component of $\nabla \times \mathbf{B}$ is shown and the vector field arrows represent the projection of the \mathbf{B} -field onto the plane. The green curve represents the intersection of the $\rho = 1$ surface and the plane and the cyan curves are the same but for $\rho = 0.8, 1.2$. In panel (b), a map of the plasma β is displayed with the \mathbf{B} -field vector arrows superimposed on top. In panel (c), a map of u_z is displayed, again with the vector arrows of the \mathbf{B} -field superimposed on top.

at $x \approx -20$, there is a thin region of strong downward pointing magnetic field, indicative of the serpentine behaviour visualized in Figure 2(f).

Figure 5(b) shows a map of the plasma β ($= 2p/|\mathbf{B}|^2$) and vector arrows of the in-plane magnetic field. In the region just below the photosphere at $x \approx -15$, the plasma β varies between 2 and 8, with a complex mixing pattern that suggests a competition for dominance between the plasma and magnetic forces. The plasma β is significantly low for part of the region in which there is a strong downward pointing field at $x \approx -20$. This value, however, quickly shifts to a much higher plasma β even where the magnetic field is still strong. This suggests that plasma motions (due to convection) are pulling down magnetic loops.

This conclusion is backed by the behaviour displayed in Figure 5(c), which displays a map of u_z and the in-plane \mathbf{B} -vectors. In the thin region of downward-pointing field at $x \approx -20$, there are strong downward flows coincident with the location where the plasma β rises sharply. In the mixed current region at $x \approx -15$, there is a strong correlation between the vertical component of the magnetic field and the sign of u_z , where $\beta \approx 5$. This evidence points strongly

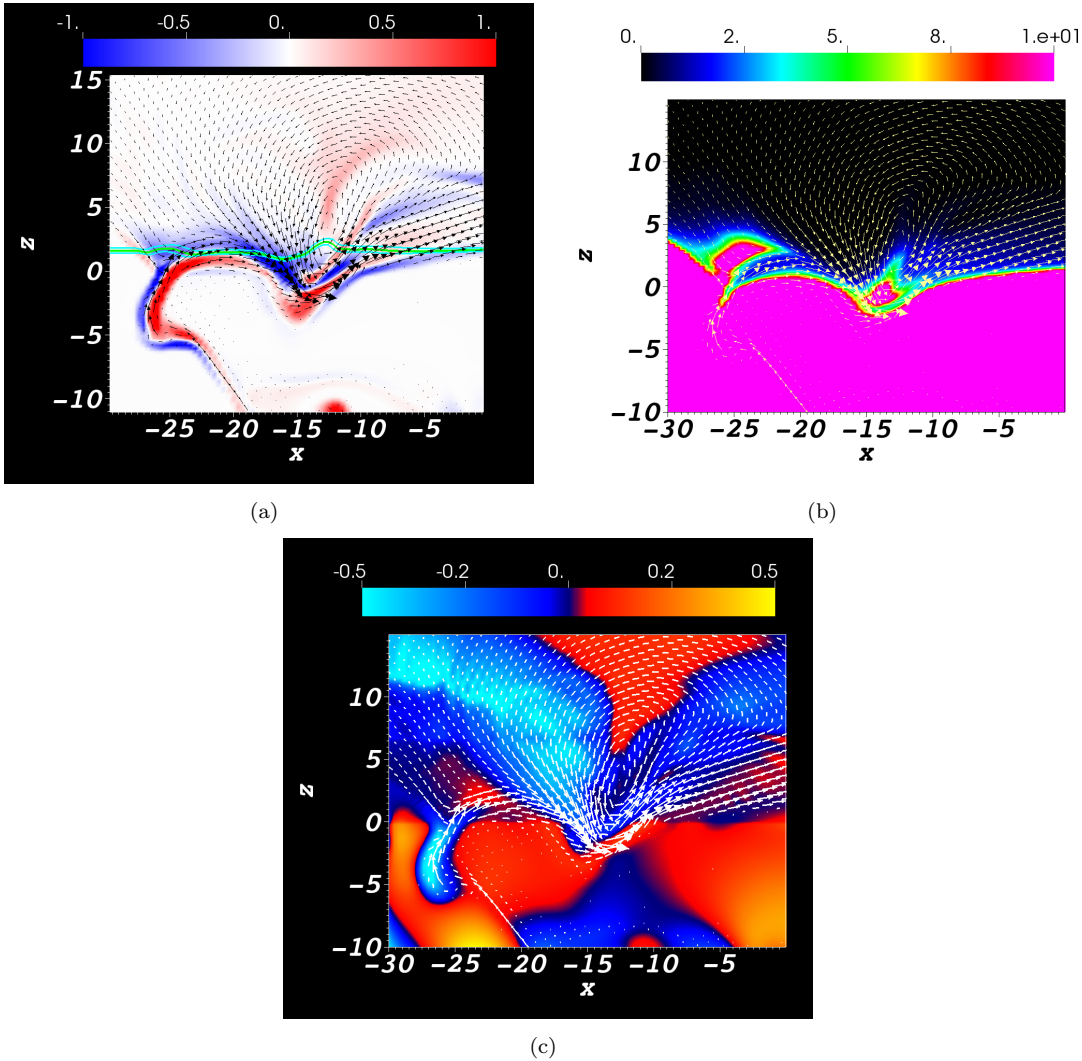
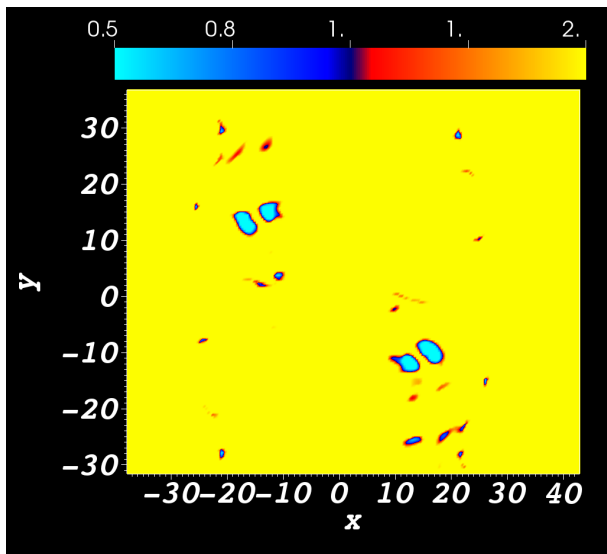


Figure 6. Slices at $t = 76$ taken in the x - z plane at $y = 10$ which intersects a region of strong negative helicity input rate $d\mathcal{H}(\mathbf{a}_0)/dt$ in Figure 4(d). In (a), a map of the y -component of $\nabla \times \mathbf{B}$ is shown and the vector field arrows represent the projection of the in-plane \mathbf{B} -field. The green curve represents the intersection of the $\rho = 1$ surface and the plane and the cyan curves are the same but for $\rho = 0.8, 1.2$. In panel (b), a map of the plasma β is displayed with the \mathbf{B} -field vector arrows superimposed on top. In panel (c), a map of u_z is displayed, again with the vector arrows of the \mathbf{B} -field superimposed on top.

to plasma motions in the convectively unstable layer generating the topological complexity of the later-stage magnetic field evolution.

Figure 6 shows the same quantities (in the same format) as Figure 5 for $y = 10$. This slice corresponds to a region of strong negative helicity rate density, as shown in Figure 4(d). In Figure 6(a), the flux rope core is found at the photospheric boundary at $x \approx -13$. Below the photospheric boundary, there are strong currents of both signs, similar to the situation at $y = 30$ in Figure 5. At $x \approx -25$ and below the flux tube core there is a strong upward-pointing magnetic field (more distorted and with more complex current structure than in the $y = 30$ case) that is another example of the serpentine loop structure. In Figure 6(b), there is a ‘pocket’ of very strong plasma β at the base of the flux tube core at the photosphere. In Figure 6(c), the vertical direction of the magnetic field correlates strongly with the direction of u_z . Also, to the left of the twisted core, magnetic field is being pulled down in a similar way to the case at $y = 30$. These results add weight to our claim that convection is primarily responsible for the increased topological complexity with time. Further, the flux rope core



(a)

Figure 7. A distribution of density in the plane $z = 0$ at $t = 76$. Regions of low density correspond to downward spikes in the surface of $\rho = 1$.

itself behaves in a serpentine manner, being both fully emerged and submerged at various locations.

One less obvious feature of the helicity rate density maps is the appearance of small bipoles. We will now focus on one of these features at $y = 14$, just above the region of strong negative $d\mathcal{H}(\mathbf{a}_0)/dt$ (see Figure 4(d)). As shown in Figure 7, the region of interest corresponds to two regions of much lower density (on the $z = 0$ plane) compared to the surrounding area. These two regions indicate downward spikes in the photospheric boundary exactly where the serpentine field enters and leaves the photosphere. A careful comparison of the helicity rate distribution in Figure 4(d) with Figure 7 reveals a number of places where there are small-scale pairs of opposing helicity input rates coinciding with paired regions of lower density.

Figure 8 displays slices at $y = 14$ and has exactly the same format as Figures 5 and 6. In Figure 8(a), the photospheric boundary dips significantly around the central twisted core, which is almost completely below the photospheric boundary. From Figure 8(b), the plasma β at the twisted core is high compared to the two dips either side of it, where there is very low plasma β and relatively strong upward and downward pointing magnetic field. Figure 8(c) confirms that the dips on either side of the core are being pulled down. The bipolar signature in the helicity rate maps can now be understood with reference to the field line emergence velocity in equation (20), namely $-u_z \mathbf{B}_{\parallel} / B_z$. With $|\mathbf{B}_{\parallel}| > 0$ and $u_z < 0$ for both dips, the changing sign of B_z in the dips results in the observed bipolar structure.

All of the features that we have investigated in this section point strongly towards convection deforming the magnetic field and changing the behaviour of the helicity input. At the start of emergence, the tube is affected by convection but is still strong enough to resist significant deformation. Later, as the field expands into the atmosphere, it becomes weaker and thus more prone to deformation by convection (in combination with other common effects associated with emergence, such a plasma drainage).

4.1.2. Winding spikes

The first spike in the winding rate series in Figure 1(c) at $t = 34$, which is negative, can be traced to the arrival of the flux tube's core at the photosphere. Figure 9 displays the winding rate distribution $d\mathcal{L}(\mathbf{a}_0)/dt$ at $t = 35$, just after the spike in the winding series. There is a clear

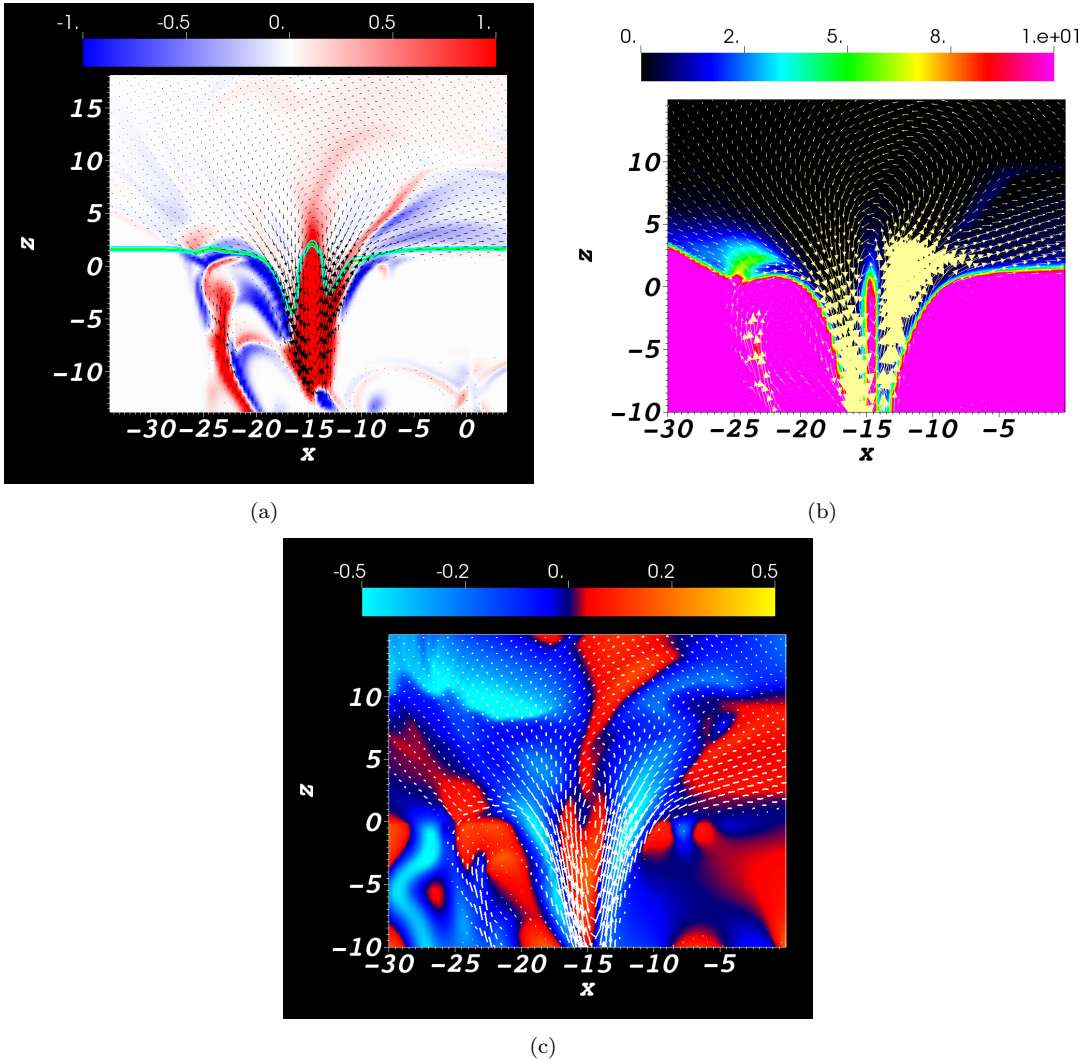


Figure 8. Slices at $t = 76$ taken in the x - z plane at $y = 14$ which intersects a region of bipolar helicity input rate $d\mathcal{H}(\mathbf{a}_0)/dt$ in Figure 4(d). In (a), a map of the y -component of $\nabla \times \mathbf{B}$ is shown and the vector field arrows represent the projection of the in-plane \mathbf{B} -field. The green curve represents the intersection of the $\rho = 1$ surface and the plane and the cyan curves are the same but for $\rho = 0.8, 1.2$. In panel (b), a map of the plasma β is displayed with the \mathbf{B} -field vector arrows superimposed on top. In panel (c), a map of u_z is displayed, again with the vector arrows of the \mathbf{B} -field superimposed on top.

sigmoidal band of negative winding rate input that corresponds to the twisted core reaching the photosphere (we will show that this is the case in more detail shortly). This clear signal of the twisted core is not clearly visible at this stage in the $d\mathcal{H}(\mathbf{a}_0)/dt$ maps, since the magnetic flux of the twisted core at the photosphere, at this stage, is relatively weak compared to later times.

What is observed in Figure 9 that is not seen in the helicity rate maps, is a clear signature in the convection cells far from the active region. Weak magnetic field carried far from the tube by convection is detected by the winding signature, with positive winding dominant in the lanes between cells and negative winding on the cell faces.

Returning to the twisted core, a similar spike in the winding rate was observed in Prior and MacTaggart (2019). In that study the spike was found to correlate with a sharp drop in the $\rho = 1$ photospheric surface, spatially localized in the region of the core. In Figure 10(a), which corresponds to $t = 34$ at $y = 0$, we see the twisted core of the magnetic field at the photosphere. In Figures 10(b-d), we see the evolution of the $\rho = 1$ photospheric surface from

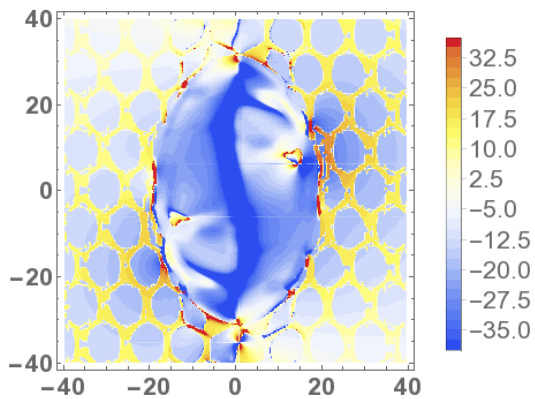


Figure 9. The distribution of $d\mathcal{L}(\mathbf{a}_0)/dt$ on the photospheric boundary at $t = 35$.

$t = 33-35$. From $t = 33$ to $t = 34$ there is a significant sharpening of the peak of the $\rho = 1$ curve, which would correspond to a relatively large effective input of negatively twisted field. From $t = 34$ to $t = 35$, the change is much less significant (although an additional disjoint surface forms). The evidence from Figures 9 and 10 confirms that the first winding rate spike in Figure 1(c) corresponds to the emergence of the twisted core just above the photospheric boundary.

In the non-convective simulation of Prior and MacTaggart (2019), there was one significant spike in the winding rate time series, corresponding to the twisted core passing the photospheric boundary. After this event, there were no more significant spikes, which indicates that no more field with significant topological complexity crossed the photosphere. In the present work, however, this is not the case and there are several spikes, both positive and negative, in the winding rate time series. By comparing Figures 1(a) and (c), the second large winding rate spike is coincident with the turning point in the helicity rate. We established earlier that the change from negative to positive growth in the helicity time series is due to the effects of convection having a growing influence in deforming the flux tube. All the winding rate spikes after the first are associated with the effects of convection deforming the magnetic field. None of the winding spikes after the first correspond to important large-scale dynamical effects. These spikes are due to the transport of small-scale weak field, which is topologically complex, across the photospheric boundary.

4.2. $B_0 = 5, \alpha = -0.4$

The helicity time series in Figures 11(a) and (b) are qualitatively similar to those of the $B_0 = 7$ case. The bulk of the input is negative, corresponding to the left-handed twisted flux tube, with a switch to positive input after $t = 70$. Again, we will show that this turning point in the helicity input series is due to the effects of convection.

In the winding time series in Figures 11(c) and (d), there are some clear differences between the series with and without the cut-off. There are also significant differences between these series and those of the $B_0 = 7$ case. We will examine the winding series in more detail but first, we present an overview of the global behaviour of emergence, as we did for the $B_0 = 7$ case.

Figure 12 displays snapshots of magnetic field lines during various stages of emergence (the format is the same as Figure 2). The general evolution, at first glance, is very similar to that of the $B_0 = 7$. The development of serpentine field lines is particularly clear in Figure 12(f).

Figure 13 displays maps of the field line helicity input rate $d\mathcal{H}(\mathbf{a}_0)/dt$ at various times during emergence. Again, the overall evolution is very similar to the $B_0 = 7$ case, as shown

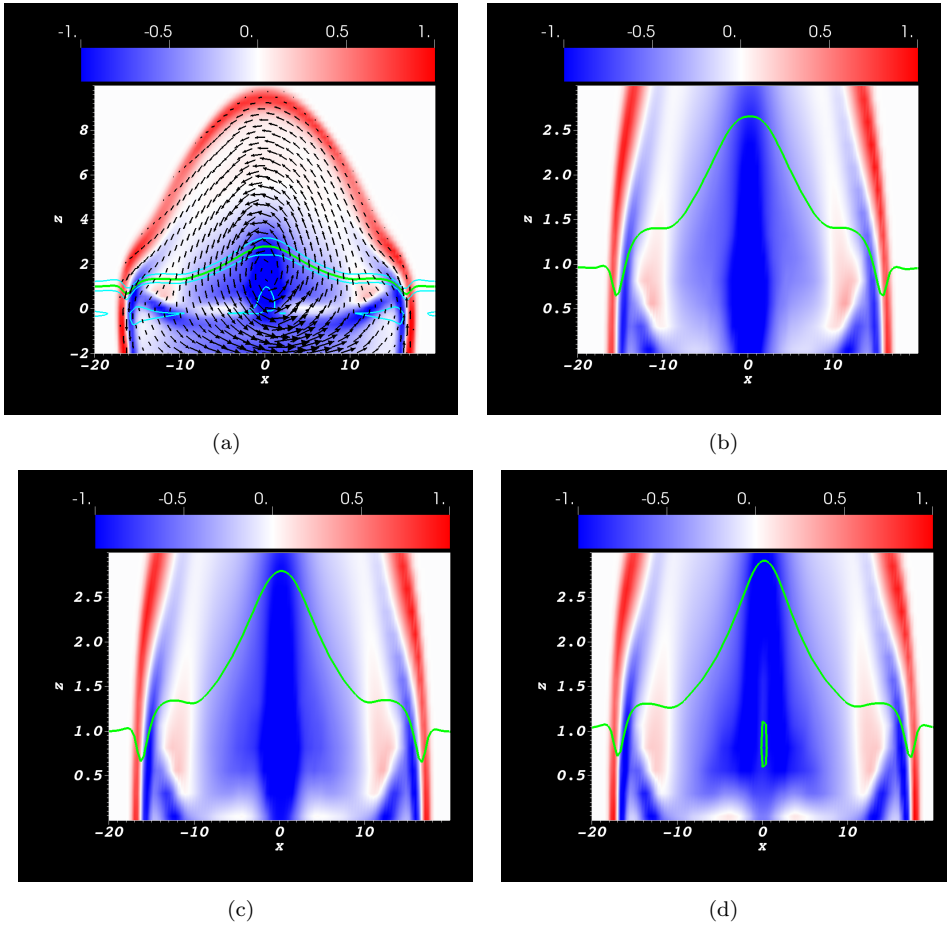


Figure 10. Slices depicting maps of $\mathbf{B} \cdot \mathbf{e}_y$ and the photospheric surface over the period $t = 33, 34, 35$ covering the first significant spike in winding input rate dL/dt seen in Figure 1(c). All figures are slices with normal \mathbf{e}_y at $y = 0$. Panel (a) shows the in-plane field component at $t = 34$, the time of the spike. Curves indicating the intersection of the plane with the photospheric surfaces $\rho = 0.8, 1, 1.2$ are also indicated. The upper part of the field's core is in the photospheric region. Panels (b)-(d) are close-ups of the $\rho = 1$ curve at $t = 33, 34, 35$ respectively.

in Figure 4. Compared to the $B_0 = 7$ case, the flux tube has weaker field strength and takes longer to reach the photosphere. Both these facts allow convection to deform the magnetic field to a greater extent than the $B_0 = 7$ case. We now investigate the greater effect of convection on the $B_0 = 5$ case compared to the $B_0 = 7$ case.

4.2.1. Winding behaviour

In Figure 1(c) of the $B_0 = 7$ case, the first spike in the winding rate time series is due to the arrival of the twisted core at the photospheric boundary. This event corresponds to a jump in the winding input in Figure 1(d). In Figure 11(c), there is a positive spike at $t = 32$, whose magnitude is reduced greatly once the cut-off is applied. Focussing on the time series with the cut-off, the winding rate becomes negative after this spike and remains negative for the rest of the simulation time. The winding input gradually becomes more negative, with one large ‘jump’ at $t = 69$ which we will return to shortly. The confusing signature of a positive spike at $t = 32$ with no cut-off and a change from zero to negative input with the cut-off, can be explained by considering the maps of $d\mathcal{L}(\mathbf{a}_0)/dt$ shown in Figure 14.

In Figure 14(a) at $t = 32$ (just before the positive spike in Figure 11(c)), the (negative) twisted core can be seen in an expanded convection cell. There are also many positive signatures, however, due to the greater influence of convection. These positive winding rates have strong enough values to dominate the winding and helicity rates in this period, leading to net

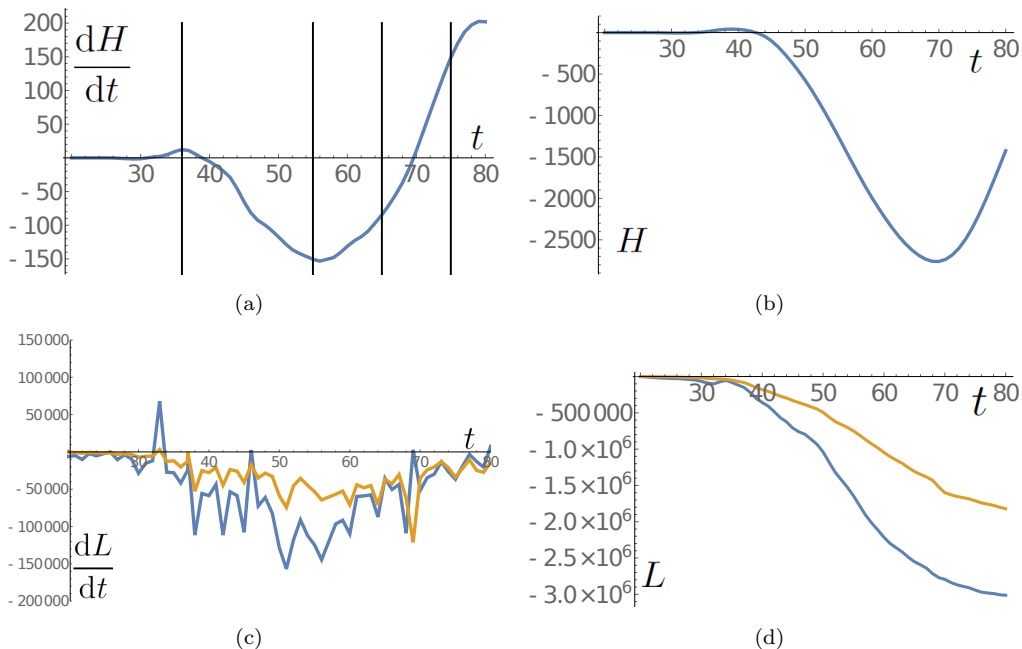


Figure 11. Helicity and winding time series for the $B_0 = 5$ $\alpha = -0.4$ case. Panel (a) shows the helicity input rate dH/dt . The vertical lines indicate times at which maps of $d\mathcal{H}(\mathbf{a}_0)/dt$ are plotted in Figure 13. Panel (b) shows the integrated helicity $H(t)$ over the same period. Panel (c) displays the winding input rate dL/dt with no cut-off (blue) and with a cut-off below $|B_z| = 0.01$ (brown). Panel (d) displays the total winding input $L(t)$.

positive inputs in both quantities. When the cut-off is included, however, almost all of these positive winding rates are removed from the calculation.

As the flux tube continues to rise and flux begins to pile up at the photosphere, the winding and helicity then both become negative. In Figure 14(b) at the later time of $t = 41$, enough of the twisted core has reached the photosphere in order to produce a signature similar to that in Figure 9 for the $B_0 = 7$ case. The arrival of the twisted core at the photosphere is also more gradual compared to the $B_0 = 7$ case. Hence, there is no obvious jump in the winding input in Figure 11(d) as there was in Figure 1(d).

At $t = 69$ in Figure 11(c), the winding rate time series, with and without the cut-off, diverge in their behaviour. The series without the cut-off becomes more positive, whereas the other becomes more negative and produces a visible jump in the winding input in Figure 11(d). Comparison with Figure 11(b) shows that the behaviour in the winding input at $t = 69$ is almost coincident with the turning point in the helicity input, which is related to the growing development of serpentine field structures. Upon investigation, we find that the behaviour of the winding input at this time does not correspond to any significant dynamical effect. In short, convection acts to distort some weak but topologically complicated magnetic field. As this field passes the photosphere, its topological signature is picked up by the winding. This rapidly changing behaviour is noticeably absent from the helicity input, which includes a weighting of magnetic flux. This event shows that although the winding signature can reveal more detailed information in conjunction with the helicity, the physical importance of the winding output requires careful analysis.

4.2.2. Serpentine core

As for the $B_0 = 7$ case, the core of the $B_0 = 5$ case flux tube also develops a serpentine structure. In Figures 13(c) and (d), the negative sigmoidal band corresponding to the twisted core appears much weaker near the centres of these maps at $(0, 0)$. The reason can be seen to be due to serpentine emergence by examining slices through the domain. Figure 15 shows

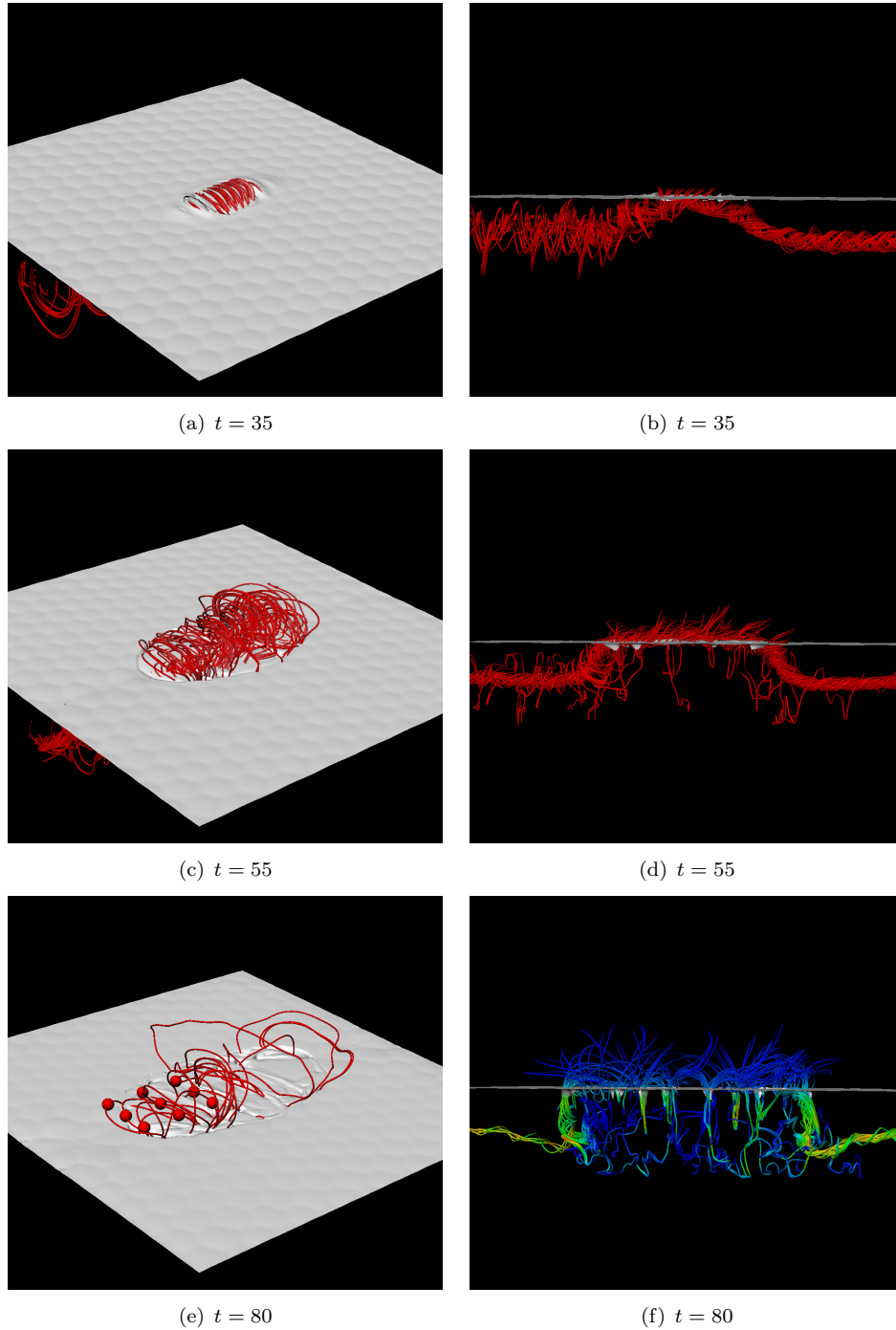


Figure 12. Field line renderings for the $B_0 = 5$ $\alpha = -0.4$ case at various points in its evolution. Panels (a) and (b) depict the field at $t = 35$. In (a) the surface shown is that of the plasma density $\rho = 1$. Panels (c) and (d) depict the field at $t = 55$. Panel (e) depicts field lines in the emerged field at $t = 80$. The spheres shown are the starting points for the field line reconstruction. Panel (f) depicts field lines side-on, with lighter colours indicating increased field strength.

two such slices. In Figure 15(a) a slice at $y = 0$ displays a map of $\mathbf{e}_y \cdot \nabla \times \mathbf{B}$ and a projection of \mathbf{B} -field vectors onto the plane. The main part of the twisted core is seen clearly above the photospheric surface (indicated by the red line). In Figure 15(b), the same variables are shown but now at $y = 10$. Here, the twisted core is held at the photospheric boundary, as suggested by Figures 13(b) and (c).

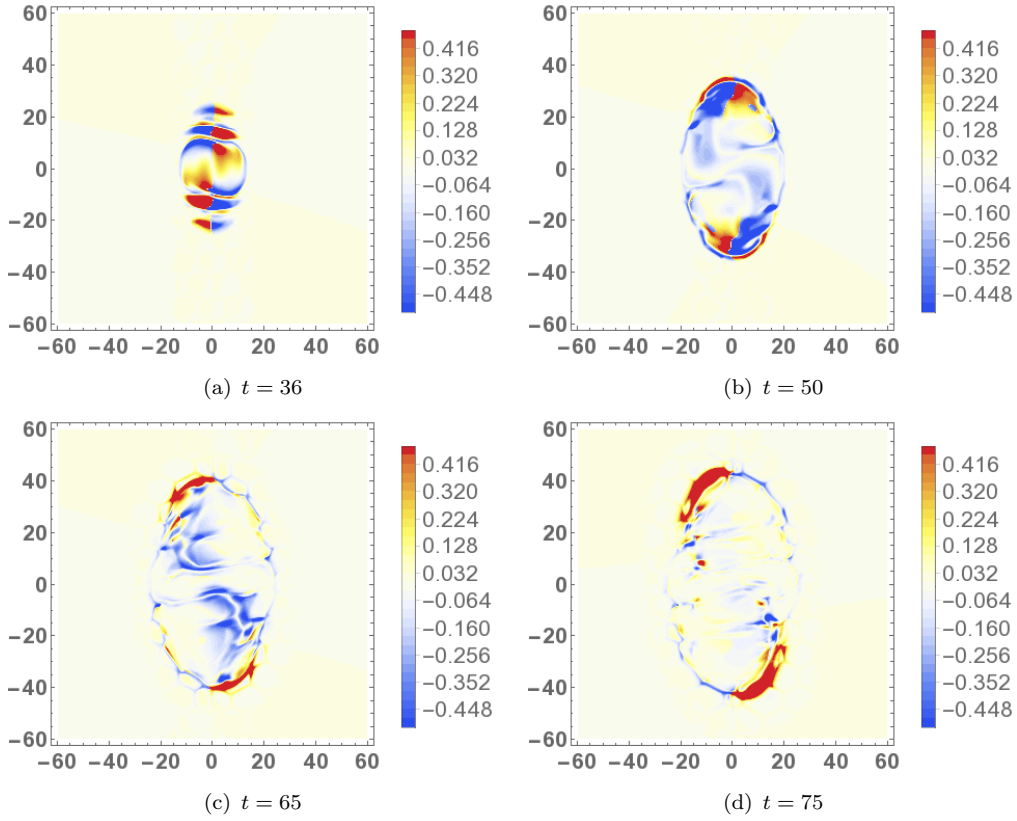


Figure 13. Helicity rate distributions at the times indicated by vertical lines in the helicity rate time series shown in Figure 11(a), i.e. $t = 36$ (a), $t = 55$ (b), $t = 65$ (c) and $t = 75$ (d).

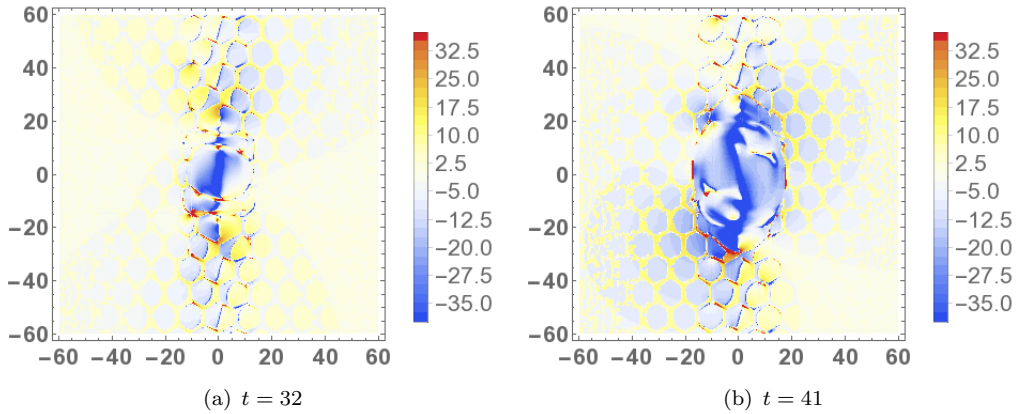


Figure 14. Maps of $d\mathcal{L}(a_0)/dt$ on the $\rho = 1$ surface at times (a) $t = 32$ and (b) $t = 41$.

4.3. $B_0 = 3$, $\alpha = -0.4$

The helicity input rate dH/dt for the $B_0 = 3$ case is shown in Figure 16(a). It is qualitatively similar to the $B_0 = 5, 7$ cases in that there is a negative helicity input rate associated with the initial emergence of the negatively twisted flux rope, which later changes to positive input. However, in this case the positive input period is much more significant than the negative input stage, as indicated by a positive net helicity input over the simulation period (Figure 16(b)). The winding rate and total input, shown in Figures 16(c) and (d) indicate, in addition to the spike of emergence of the flux tube core at the photosphere, a steady input of negative

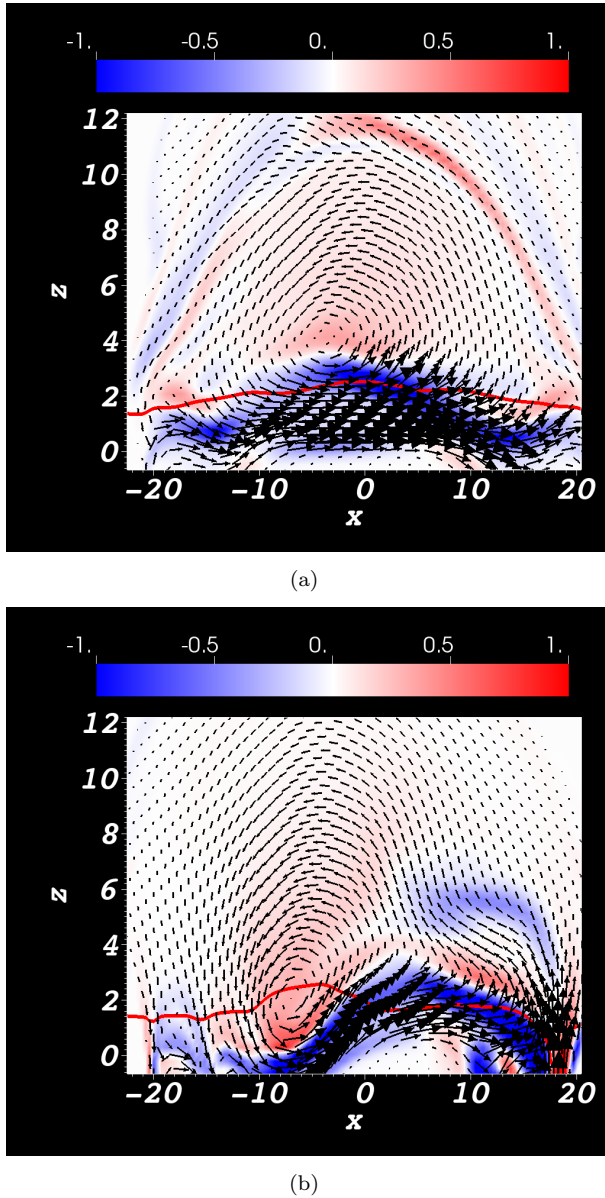


Figure 15. Slices of the $B_0 = 5$ case at $t = 55$ in the x - z plane. The density plotted is the y -component of $\nabla \times \mathbf{B}$. The red curves represent the intersection of the slices with the $\rho = 1$ surface. In (a), the intercept with the y -axis is at $y = 0$ and the tube's core is above the $\rho = 1$ line. In (b), the intercept with the y -axis is at $y = 10$ and the tube's core is centered at the $\rho = 1$ line.

field line topology. The results of Figure 16 suggest the following summary: the twisted core reaches the photosphere, inputs negative winding into the atmosphere and, due to the tube's relatively weak field strength, is deformed significantly by convection.

This conclusion is verified in Figure 17. In Figures 17(a) and (b), corresponding to $t = 55$, we see visualizations of field lines when the helicity rate has its most negative value. Here, the twisted core has reached the photosphere but the magnetic field does not emerge into the atmosphere as much as the two stronger cases. This slower emergence has also been found in non-convective models (Murray *et al.* 2006).

At $t = 75$ (Figures 17(c) and (d)) we see the formation of serpentine structures in the emerging field, similar to the $B_0 = 5, 7$ cases. By $t = 98$ (Figures 17(e) and (f)) the field has emerged much more extensively into the transition region and retains a significantly complex

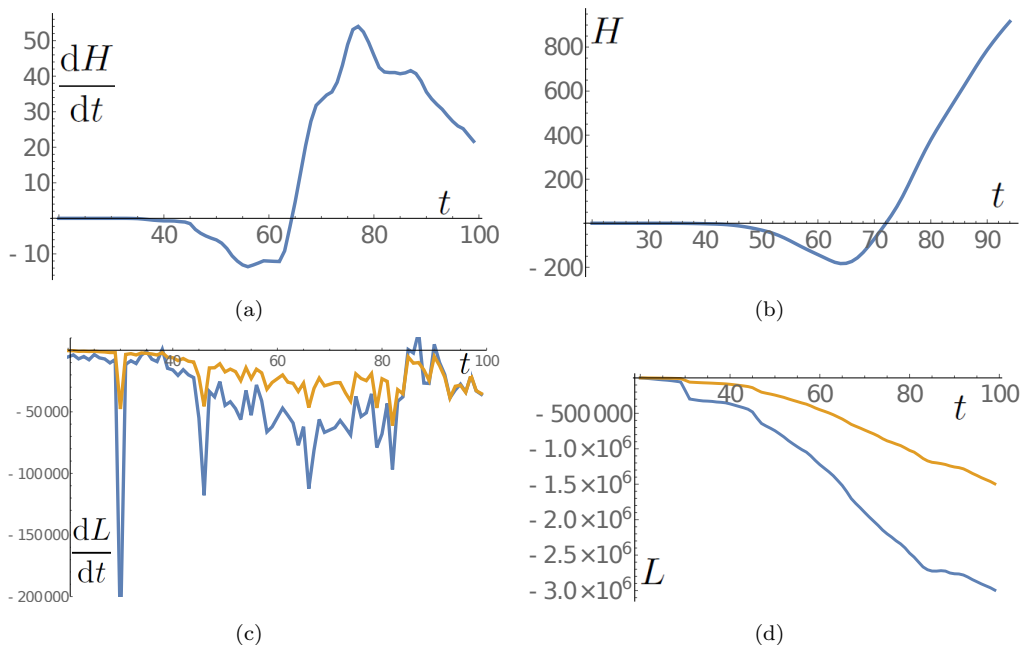


Figure 16. Helicity and winding time series for the $B_0 = 3 \alpha = -0.4$ case. Panel (a) shows the helicity input rate dH/dt . Panel (b) shows the integrated helicity $H(t)$ over the same period. Panel (c) displays the winding input rate dL/dt with no cut-off (blue) and with a cut-off below $|B_z| = 0.01$ (brown). Panel (d) displays the total winding input $L(t)$.

serpentine like structure. In Figure 17(f), regions of strong field strength can be seen clearly beneath dips in the photospheric surface. These features are clear signatures of how convection deforms the magnetic field, particularly for this weaker tube.

4.4. Fixed photosphere

As stated earlier, we now show an example of the helicity and winding time series calculated using a fixed planar photosphere at $z = 0$. The results are shown in Figure 18.

The helicity time series in Figures 18(a) and (b) are qualitatively similar to the moving-photosphere case. The winding time series in Figures 18(c) and (d) show some clearer differences. Focusing on the winding input series in Figure 18(d), there are two main phases. The first phase ends at $t \approx 40$ and represents weak field from the top of the emerging flux tube reaching the $z = 0$ plane. After $t \approx 40$, the winding input rate becomes faster, with many spikes in Figure 18(c), until the winding input effectively levels off. The start of this phase corresponds to increased negative helicity input in Figure 18(b) and represents the main core of the flux tube passing the photosphere. Once most of the twisted flux tube has passed the $z = 0$, there is no more topological input above this plane and the winding input levels off. This picture is similar to the situation found in the no-convective simulation of Prior and MacTaggart (2019).

Although the winding time series with and without the cut-off are qualitatively similar, there are significant quantitative differences. This example shows the importance of testing the winding results using cut-off thresholds.

5. Summary and discussion

In this work we have analyzed helicity and winding fluxes in simulations of twisted flux tube emergence with a range of different initial field strengths. In particular, we have focused on

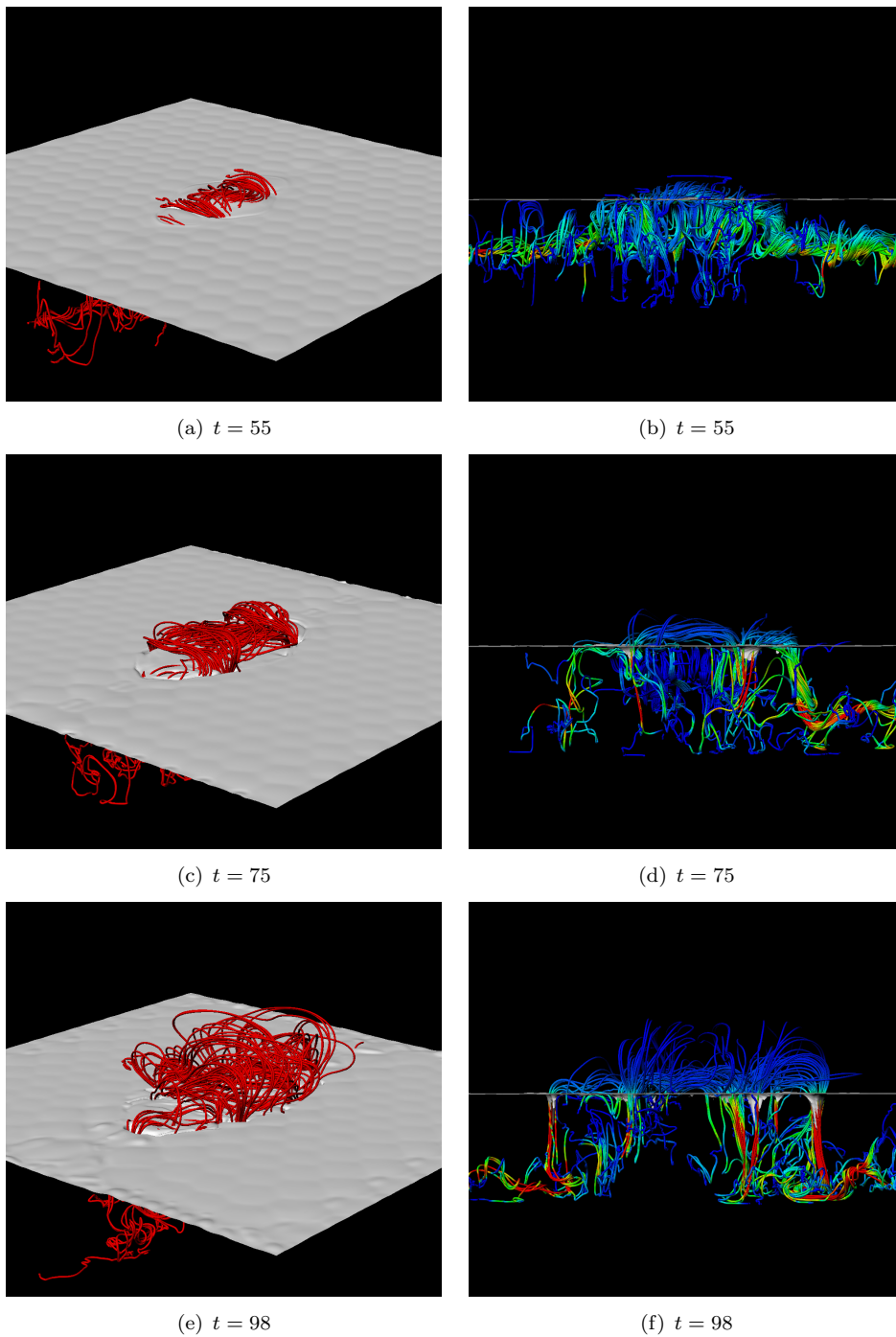


Figure 17. Field line renderings for the $B_0 = 3$ $\alpha = -0.4$ field emergence at various points in its evolution. Panels (a) and (b) depict the field at $t = 55$. In (a) the surface shown is that of the plasma density $\rho = 1$. Panels (c) and (d) depict the field at $t = 75$. Panel (e) depicts field lines in the emerged field at $t = 98$. In panels (b), (d) and (f), the field lines are coloured by field strength with lighter colors indicating increased strength.

the effect of convection on the topological quantities and have compared the results to those of other work that does not include convection. In the present study, we can pick out some general results:

1. Convective flows act to pull down sections of the emerging field, leading to a more complex serpentine field line connectivity at the photospheric surface than typically

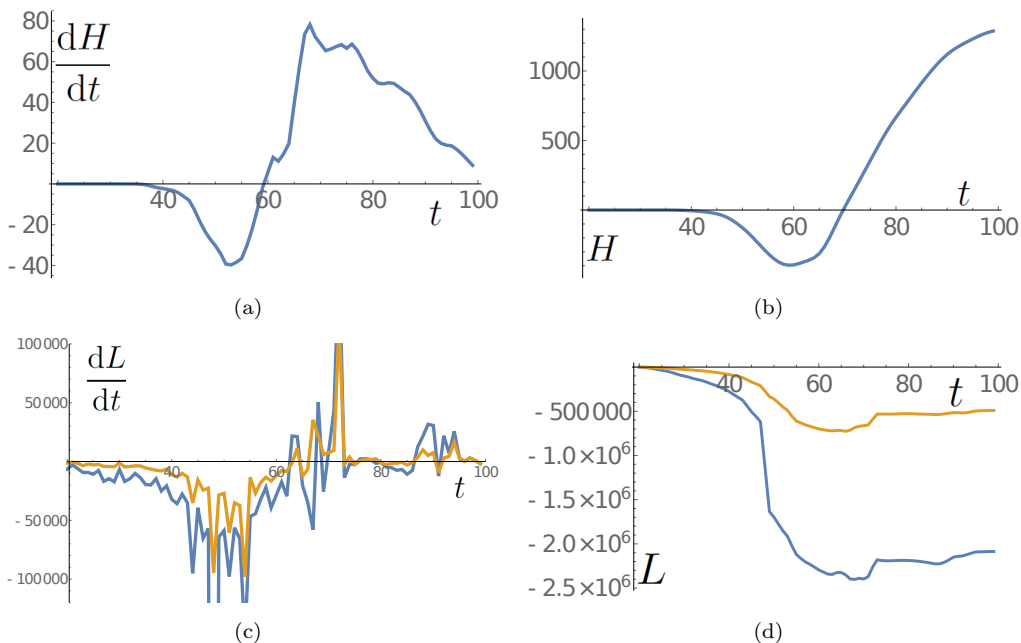


Figure 18. Helicity and winding time series for the $B_0 = 3$ $\alpha = -0.4$ case using the field sampled at the surface $z = 0$ (\mathbf{B}^F and \mathbf{u}^F). Panel (a) shows the helicity input rate dH/dt . Panel (b) displays the integrated helicity $H(t)$ over the same period. Panel (c) shows the winding input rate dL/dt with no cut-off (blue) and with a cut-off below $|B_z| = 0.01$ (brown). Panel (d) shows the total winding input $L(t)$.

observed for non-convective flux rope simulations. This effect also leads to a reversal in sign of the rate of helicity input dH/dt . In the case of the weaker magnetic field strengths, this effect further acts to lead to a change in sign of the *net* helicity input $H(t)$. Thus mixed input time series can be produced by single sign helicity flux ropes if convection is accounted for. The strength of the field appears to dictate the degree of this serpentine structure and its effect on the helicity input series.

2. As was found in Prior and MacTaggart (2019), the winding input rate time series tends to exhibit spikes when structures of significant topology pass into the photospheric region. With the inclusion of convection in the model, the winding signature still provides a clear signature for the arrival of the twisted core at the photosphere and, therefore, the emergence of twisted field into the solar atmosphere. A combination of winding time series and distributions can be used to establish this signature.
3. The winding input rate dL/dt and net input rate $L(t)$, which are independent of any magnetic field strength weighting, are not so influenced by the general downward pulling of the field by convective flows. Thus the winding series generally show a steady input of negative topology, concordant with the flux tube's initial structure.
4. Some spikes in the winding rate time series correspond to small parts of the magnetic field which, although have a complex field line topology, are insignificant dynamically. Care must be taken when calculating winding signatures and it is important to cross-reference results from time series with distributions of $d\mathcal{L}(\mathbf{a}_0)/dt$ and other helicity results.
5. Analyzing helicity and winding signatures together provides a much more detailed picture of the initial stages of active region emergence into the solar atmosphere.

Throughout this work we have made comparisons to the non-convective emergence simulation in Prior and MacTaggart (2019). Although the behaviour of emergence in this work exhibits significant differences compared to that in Prior and MacTaggart (2019), the applicability of both helicity and winding signatures in identifying key events, still holds. In

particular, the field line winding continues to give a clear signal of the arrival of twisted field in the solar atmosphere.

We plan to extend this work in three directions. The first is to analyze the helicity and winding rates in observations and, in particular, determine early-warning signatures for possible eruptions. The second is to study the topological signatures of the emergence of magnetic field structures different from twisted flux tubes, such as ‘mixed helicity’ fields (Prior and MacTaggart 2019). The third avenue that we will pursue is to examine how helicity and winding signatures can be used to interpret more advanced stages of emergence, including the onset of eruptions.

Results were obtained using the ARCHIE-WeSt High Performance Computer (www.archie-west.ac.uk) based at the University of Strathclyde.

References

- Abbett, W.P., Fisher, G.H., Fan, Y. and Bercik, D.J., The Dynamic Evolution of Twisted Magnetic Flux Tubes in a Three-dimensional Convecting Flow. II. Turbulent Pumping and the Cohesion of Ω -Loops. *Astrophysical Journal*, 2004, **612**, 557.
- Arber, T., Longbottom, A., Gerrard, C. and Milne, A., A staggered grid, Lagrangian–Eulerian remap code for 3-D MHD simulations. *Journal of Computational Physics*, 2001, **171**, 151.
- Archontis, V. and Hood, A.W., Formation of Ellerman bombs due to 3D flux emergence. *Astronomy & Astrophysics*, 2009, **508**, 1469.
- Archontis, V., Hood, A.W., Savcheva, A., Golub, L. and Deluca, E., On the Structure and Evolution of Complexity in Sigmoids: A Flux Emergence Model. *Astrophysical Journal*, 2009, **691**, 1276.
- Berger, M.A., Rigorous new limits on magnetic helicity dissipation in the solar corona. *Geophysical and Astrophysical Fluid Dynamics*, 1984, **30**, 79.
- Berger, M.A., An energy formula for nonlinear force-free magnetic fields. *Astronomy & Astrophysics*, 1988, **201**, 355.
- Brandenburg, A., Kleorin, N. and Rogachevskii, I., Large-scale magnetic flux concentrations from turbulent stresses. *Astronomische Nachrichten*, 2010, **331**, 5.
- Bushby, P.J. and Archontis, V., Modelling magnetic flux emergence in the solar convection zone. *Astronomy & Astrophysics*, 2012, **545**, A107.
- Chae, J., Observational determination of the rate of magnetic helicity transport through the solar surface via the horizontal motion of field line footpoints. *Astrophysical Journal Letters*, 2001, **560**, L95.
- Chae, J., Moon, Y.J. and Park, Y.D., Determination of magnetic helicity content of solar active regions from SOHO/MDI magnetograms. *Solar Physics*, 2004, **223**, 39.
- Chandrasekhar, S., *Hydrodynamic and hydromagnetic stability*, 1961 (Oxford University Press).
- Cheung, M.C.M. and Isobe, H., Flux Emergence (Theory). *Living Reviews in Solar Physics*, 2014, **11**, 3.
- Christopherson, D.G., Note on the vibration of membranes. *The Quarterly Journal of Mathematics*, 1940, **11**, 63.
- Cowling, T.G., The growth and decay of the sunspot magnetic field. *Monthly Notices of the Royal Astronomical Society*, 1946, **106**, 218.
- Démoulin, P. and Berger, M.A., Magnetic Energy and Helicity Fluxes at the Photospheric Level. *Solar Physics*, 2003, **215**, 203.
- Fan, Y., The Emergence of a Twisted Ω -Tube into the Solar Atmosphere. *Astrophysical Journal Letters*, 2001, **554**, L111.
- Fan, Y., Abbett, W.P. and Fisher, G.H., The Dynamic Evolution of Twisted Magnetic Flux Tubes in a Three-dimensional Convecting Flow. I. Uniformly Buoyant Horizontal Tubes. *Astrophysical Journal*, 2003, **582**, 1206.
- Fan, Y. and Gibson, S., Numerical simulations of three-dimensional coronal magnetic fields resulting from the emergence of twisted magnetic flux tubes. *Astrophysical Journal*, 2004, **609**, 1123.
- Harra, L., Magara, T., Hara, H., Tsuneta, S., Okamoto, T. and Wallace, A., Response of the solar atmosphere to the emergence of serpentine magnetic field. *Solar Physics*, 2010, **263**, 105.
- Hood, A.W., Archontis, V. and MacTaggart, D., 3D MHD Flux Emergence Experiments: Idealised Models and Coronal Interactions. *Solar Physics*, 2012, **278**, 3.
- Jensen, E., On tubes of magnetic forces embedded in stellar material. *Annales d’Astrophysique*, 1955, **18**, 127.

- Kemel, K., Brandenburg, A., Kleorin, N., Mitra, D. and Rogachevskii, I., Active Region Formation through the Negative Effective Magnetic Pressure Instability. *Solar Physics*, 2013, **287**, 293.
- Kusano, K., Maeshiro, T., Yokoyama, T. and Sakurai, T., Measurement of magnetic helicity injection and free energy loading into the solar corona. *Astrophysical Journal*, 2002, **577**, 501.
- Leake, J.E. and Arber, T.D., The emergence of magnetic flux through a partially ionised solar atmosphere. *Astronomy & Astrophysics*, 2006, **450**, 805.
- MacTaggart, D. and Hood, A.W., On the emergence of toroidal flux tubes: general dynamics and comparisons with the cylinder model. *Astronomy & Astrophysics*, 2009, **507**, 995.
- Mitra, D., Brandenburg, A., Kleorin, N. and Rogachevskii, I., Intense bipolar structures from stratified helical dynamos. *Monthly Notices of the Royal Astronomical Society*, 2014, **445**, 761.
- Moraitis, K., Tziotziou, K., Georgoulis, M.K. and Archontis, V., Validation and benchmarking of a practical free magnetic energy and relative magnetic helicity budget calculation in solar magnetic structures. *Solar Physics*, 2014, **289**, 4453.
- Muller, R., A model of photospheric faculae deduced from white light high resolution pictures. *Solar Physics*, 1975, **45**, 105.
- Murray, M.J., Hood, A.W., Moreno-Insertis, F., Galsgaard, K. and Archontis, V., 3D simulations identifying the effects of varying the twist and field strength of an emerging flux tube. *Astronomy & Astrophysics*, 2006, **460**, 909.
- Pariat, E., Using Magnetic Helicity, Topology, and Geometry to Investigate Complex Magnetic Fields; in *Topics in Magnetohydrodynamic Topology, Reconnection and Stability Theory*, edited by D. MacTaggart and A. Hillier, 2019, p. 145.
- Pariat, E., Aulanier, G., Schmieder, B., Georgoulis, M.K., Rust, D.M. and Bernasconi, P.N., Resistive Emergence of Undulatory Flux Tubes. *Astrophysical Journal*, 2004, **614**, 1099.
- Pariat, E., Démoulin, P. and Berger, M.A., Photospheric flux density of magnetic helicity. *Astronomy & Astrophysics*, 2005, **439**, 1191.
- Pariat, E., Masson, S. and Aulanier, G., Current buildup in emerging serpentine flux tubes. *Astrophysical Journal*, 2009, **701**, 1911.
- Parker, E.N., The Formation of Sunspots from the Solar Toroidal Field. *Astrophysical Journal*, 1955, **121**, 491.
- Poisson, M., Démoulin, P., López Fuentes, M. and Mandrini, C.H., Properties of Magnetic Tongues over a Solar Cycle. *Solar Physics*, 2016, **291**, 1625.
- Poisson, M., Mandrini, C.H., Démoulin, P. and López Fuentes, M., Evidence of Twisted Flux-Tube Emergence in Active Regions. *Solar Physics*, 2015, **290**, 727.
- Priest, E., *Magnetohydrodynamics of the Sun*, 2014 (Cambridge University Press).
- Prior, C. and MacTaggart, D., Interpreting magnetic helicity flux in solar flux emergence. *Journal of Plasma Physics*, 2019, **85**.
- Prior, C. and Yeates, A.R., Quantifying reconnective activity in braided vector fields. *Physical Review E*, 2018, **98**, 013204.
- Sturrock, Z. and Hood, A.W., Sunspot rotation-II. Effects of varying the field strength and twist of an emerging flux tube. *Astronomy & Astrophysics*, 2016, **593**, A63.
- Valori, G., Green, L.M., Démoulin, P., Domínguez, S.V., van Driel-Gesztelyi, L., Wallace, A., Baker, D. and Fuhrmann, M., Nonlinear force-free extrapolation of emerging flux with a global twist and serpentine fine structures. *Solar Physics*, 2012, **278**, 73.
- Van Leer, B., Towards the ultimate conservative difference scheme. V. A second-order sequel to Godunov's method. *Journal of Computational Physics*, 1979, **32**, 101.
- Vemareddy, P. and Démoulin, P., Successive injection of opposite magnetic helicity in solar active region NOAA 11928. *Astronomy & Astrophysics*, 2017, **597**, A104.
- Wilkins, M.L., Use of artificial viscosity in multidimensional fluid dynamic calculations. *Journal of computational physics*, 1980, **36**, 281.
- Yang, S., Büchner, J., Santos, J.C. and Zhang, H., Evolution of relative magnetic helicity: method of computation and its application to a simulated solar corona above an active region. *Solar Physics*, 2013, **283**, 369.